

SHELS: TESTING WEAK LENSING MAPS WITH REDSHIFT SURVEYS

Margaret J. Geller

*Smithsonian Astrophysical Observatory,
60 Garden St., Cambridge, MA 02138*

`mgeller@cfa.harvard.edu`

Michael J. Kurtz

*Smithsonian Astrophysical Observatory,
60 Garden St., Cambridge, MA 02138*

`mkurtz@cfa.harvard.edu`

Ian P. Dell’Antonio

*Department of Physics, Brown University,
Box 1843, Providence, RI 02912*

`ian@het.brown.edu`

Massimo Ramella

*INAF, Osservatorio Astronomico di Trieste,
via C. B. Tiepolo 11, I-34131 Trieste, Italy*

`ramella@ts.astro.it`

Daniel G. Fabricant

*Smithsonian Astrophysical Observatory,
60 Garden St., Cambridge, MA 02138*

`dfabricant@cfa.harvard.edu`

ABSTRACT

Weak lensing surveys are emerging as an important tool for the construction of “mass selected” clusters of galaxies. We evaluate both the efficiency and completeness of a weak lensing selection by combining a dense, complete redshift

survey, the Smithsonian Hectospec Lensing Survey (SHELS), with a weak lensing map from the Deep Lens Survey (DLS). SHELS includes 11,692 redshifts for galaxies with $R \leq 20.6$ in the four square degree DLS field; the survey is a solid basis for identifying massive clusters of galaxies with redshift $z \lesssim 0.55$. The range of sensitivity of the redshift survey is similar to the range for the DLS convergence map. Only four of the twelve convergence peaks with signal-to-noise ≥ 3.5 correspond to clusters of galaxies with $M \gtrsim 1.7 \times 10^{14} M_{\odot}$. Four of the eight massive clusters in SHELS are detected in the weak lensing map yielding a completeness of $\sim 50\%$. We examine the seven known extended cluster x-ray sources in the DLS field: three can be detected in the weak lensing map, three should not be detected without boosting from superposed large-scale structure, and one is mysteriously undetected even though its optical properties suggest that it should produce a detectable lensing signal. Taken together, these results underscore the need for more extensive comparisons among different methods of massive cluster identification.

Subject headings: galaxies: clusters: individual (CXOU J091551+293637, CXOU J091554+293316, CXOU J091601+292750, XMMU J091935+303155, A781, CXOU J09202+302938, CXOU J092053+302800, CXOU J092110+302751) — galaxies: distances and redshifts — gravitational lensing — large-scale structure of universe

1. Introduction

Weak lensing maps and redshift surveys are fundamental, complementary tools of modern cosmology. A weak lensing map provides a weighted “picture” of projected surface mass density; a redshift survey provides a three-dimensional map of the galaxy distribution resolving structures along the line of sight within the broad window “imaged” by the lensing map.

Although galaxies are biased tracers of the mass distribution, comparison of a weak lensing map with a foreground redshift survey covering the appropriate range promises progress in resolving some of the issues limiting cosmological applications of weak lensing. Here we focus on the use of weak lensing for identifying clusters of galaxies.

We compare the set of massive clusters identified in a dense, complete redshift foreground redshift survey with significant weak lensing map convergence peaks. The Smithsonian Hectospec Lensing Survey (SHELS hereafter : Geller et al. 2005) includes redshifts for 11,692 galaxies in a four square degree field of the Deep Lens Survey (Wittman et al. 2002;

DLS hereafter). SHELS enables identification of massive clusters for redshifts $z \lesssim 0.55$, the range of maximum sensitivity of the DLS. Comparison of the two surveys measures *both* the efficiency and completeness of the weak lensing map for the identification of massive clusters. These combined measures are the first direct assays for any weak lensing survey. They provide an important benchmark for future work.

1.1. History and Challenges

The construction of large catalogs of clusters of galaxies has a long history in the optical (e.g. Abell 1958; Zwicky et al. 1968; Abell et al. 1989; Koester et al. 2007) and in the x-ray (e.g. Schwarz 1978; Piccinotti 1982; Edge et al. 1990; Ebeling et al. 1996; Böhringer et al. 2004). In these approaches, the catalog selection parameters are related to the cluster mass only through scaling relations. In contrast, weak lensing offers the enticing possibility of obtaining a “(projected) mass selected” catalog of clusters directly.

Several studies show that weak lensing maps are a route to cluster identification. Wittman et al. (2001) used the Deep Lens Survey to make the first detection of a previously uncatalogued cluster from a convergence map. Subsequently Miyazaki et al. (2002, 2007), Hettterscheidt et al. (2005), Wittman et al. (2006), Schirmer et al. (2007), and Gavazzi & Soucail (2007), Hamana et al. (2008), Bergé et al. (2008), and Dietrich et al. (2008) have all demonstrated coincidence of optical and/or x-ray clusters with peaks in weak lensing convergence maps.

The number of candidate clusters identified from weak lensing maps has risen steeply to several hundred. For the two largest sets of candidates, the success rate for identifying these candidates with clusters of galaxies differs substantially. Miyazaki et al. (2007) claim an 80% success rate for the ~ 100 peaks in their convergence maps with a signal-to-noise greater than 3.69. Hamana et al. (2008) support this claim with sparse spectroscopic sampling of 36 weak lensing cluster candidates. In contrast, Schirmer et al. (2007) identified 158 possible mass concentrations in a blindly selected sample and derive a $\sim 45\%$ success rate for their $\sim 4\sigma$ convergence map peaks consistent with an earlier evaluation of a subsample of the survey (Maturi et al. 2007). The 4σ significance threshold may be an overestimate because Schirmer et al (2007) combine sets of peaks identified with two different statistics to construct their sample. A third independent analysis of convergence maps from the CFHTLS (Gavazzi & Soucail 2007) yields an intermediate $\sim 65\%$ success rate among 14 peaks identified above a signal-to-noise threshold of 3.5.

Miyazaki et al. (2007) attribute the much lower success rate of Schirmer et al. (2007) to

the generally lower source density in the Schirmer et al. (2007) weak lensing maps. However, there are other possibly important differences in the construction and analyses of the maps. Schirmer et al. (2007) include a detailed discussion of a variety of statistical issues in both the identification of convergence map peaks and of the related concentrations of galaxies. Although there are some qualitative aspects in their evaluation of the galaxy counts, they limit the identification of coincidences to apparent systems with redshifts less than ~ 0.3 . This limit is roughly consistent with their lower source density. In contrast, Miyazaki et al. (2007) and Hamana et al. (2009) claim probable coincidences to a redshift of 0.5 or more. Short of performing exactly the same analysis on the two datasets it is difficult to account for the differing success rates from consideration of the relative background source counts alone.

Miyazaki et al. (2007) use a combination of x-ray observations, redshift measurements (extended by Hamana et al. (2009)), and imaging to identify their convergence peaks with systems of galaxies. Schirmer et al. (2007) take a more uniform approach of counting galaxies in beams with a $2'$ radius around the centers of their convergence peaks; they measure the apparent overdensity in the magnitude range $R \sim 17 - 22$ and make an assessment of significance depending on the excess count (with some occasional qualitative modifications).

Gavazzi & Soucail (2007) also take a uniform approach to the evaluation of significance of the peaks; they use the distribution of photometric redshifts for galaxies in a circular aperture of $2'$ centered on each convergence peak. They subtract a background distribution computed from galaxies which lie more than $6'$ from any convergence peak. For 9 of their 14 peaks, they define the associated cluster redshift as the location of the most prominent photoz peak. One remarkable feature of the Gavazzi & Soucail analysis is the low velocity dispersion (as low as 450 km/s) for some of the systems corresponding to convergence peaks.

Most recently Kubo et al. (2009) use x-ray observations, DLS images, and available redshifts to estimate the fraction of false positives in a maximum likelihood weak lensing reconstruction. They conclude that only 10-25% of their peaks with signal-to-noise greater than 3.5 are false positives. This conclusion may be overly optimistic because they consider coincidences of peaks and apparent systems with angular separations as large as 4 arcminutes. Schirmer et al. (2007) and Gavazzi & Soucail (2007) show that the average angular offset between convergence peaks and optical counterparts is $0.9 \pm 0.5'$. The convergence maps of Schirmer et al. (2007) and Gavazzi & Soucail (2007) are sensitive to lensing systems in approximately the same redshift range as the DLS.

Recent simulations of the efficacy of convergence maps for construction of mass-selected cluster catalogs are based on ray-tracing through large n-body simulations (Hamana et al. 2004; Hennawi & Spergel 2005). Hamana et al. (2004) make a set of mock observations

where they associate convergence map peaks with halos. They conclude that for convergence peaks with a signal-to-noise > 4 , more than 60% of massive halos are detected. On the other hand, they also estimate that a conservative 40% of these convergence peaks are false positives. Although the details of the simulation differ from the observations, the estimated false positive rate is consistent with the conclusions of Gavazzi & Soucail (2007), more optimistic than Schirmer et al. (2007), and less optimistic than Miyazaki et al. (2007) or Kubo et al. (2009). The $\sim 80\%$ rate of the Miyazaki et al (2007) survey is very close to the $\sim 85\%$ maximum achievable (Hennawi & Spergel). Simulations by Dietrich et al. (2008) also show that 75% of matches between convergence map peaks and massive halos are within $2.15'$, consistent with the observational offsets observed by Schirmer et al. (2007) and Gavazzi & Soucail (2007).

In all of these recent studies some convergence peaks are associated with superpositions of several systems, often with low velocity dispersion, along the line-of-sight toward the weak lensing peak. A clean evaluation of the nature and frequency of such superpositions is very difficult without a complete foreground redshift survey. The fraction of “dark” peaks attributable to noise appears to vary with the nature of the convergence map and with the method of cross-identifying convergence peaks with physical systems. Yet another issue not considered in analyses to date is the frequency of accidental coincidences between convergence map peaks and apparent systems of galaxies. Understanding the noise properties of convergence maps and the related correspondence between the weak lensing signature and structures in the galaxy distribution is a continuing challenge (Mellier 1999; Schneider 2006).

1.2. The Importance of a Foreground Redshift Survey

A foreground redshift survey is an independent measure of the matter distribution revealed by a convergence map. Here we use a complete redshift survey, SHELS, to compare peaks in the DLS convergence map with probable systems identified in the redshift survey. We develop procedures similar to those adopted by Schirmer et al. (2007) and Gavazzi & Soucail (2007) who use narrow probes through their photometric data to evaluate coincidences between potential lensing systems and peaks in their convergence maps.

The advantages of a redshift survey for evaluating the efficiency of a lensing include (1) resolution of structures along the line-of-sight, (2) availability of a velocity dispersion, and (3) bases for constructing a control sample and evaluating false positives. Combining a redshift survey with a lensing map enables an evaluation of the frequency of chance coincidences between significant lensing peaks and systems of galaxies or halos. The redshift survey also provides an estimate of the number of systems undetected by the weak lensing map.

Consideration of these issues has previously been limited largely to simulations.

In Section 2 we describe the DLS lensing map and the SHELS redshift survey. We calculate the sensitivity of the DLS to clusters with a given rest frame line-of-sight velocity dispersion in Section 2.2. Section 3.1 develops the technique we use for evaluating the match between the convergence map peaks and structures in the redshift survey. We examine the redshift distribution along the line-of-sight toward the 12 most significant weak lensing peaks in Section 3.2 and compute rest frame line-of sight velocity dispersions for these candidate DLS/SHELS clusters in Section 3.3. We discuss the seven known extended clusters x-ray sources in Section 3.4 and construct a set of SHELS candidate clusters independent of the DLS map in Section 3.5. We evaluate the efficiency and completeness of the DLS convergence map in Section 4. In Section 5 we demonstrate the potential impact of photometric redshifts on the evaluation of the efficiency of weak lensing for massive cluster identification. Section 6 compares our results with simulations by Dietrich et al. (2008) and Hamana et al. (2004). We conclude in Section 7. We use the WMAP concordance cosmology (Spergel et al. 2007) throughout with $H_o = 73$, $\Omega_m = 0.3$ and $\Omega_\Lambda = 0.7$.

2. The Data

We use two ambitious surveys to explore the coincidence of lensing peaks with halos observed as systems of galaxies with rest-frame line-of-sight velocity dispersions $\gtrsim 600 \text{ km s}^{-1}$ or, equivalently, masses $\gtrsim 2 \times 10^{14} M_\odot$. The DLS (Wittman et al. 2002) is an NOAO key program covering 20 square degrees in five separate fields; we use the four square degree F2 field at $\alpha = 09^h 19^m 32.4^s$ and $\delta = +30^\circ 00' 00''$. SHELS is a redshift survey covering the F2 field. SHELS is 98% complete to a limiting apparent magnitude $R = 20.3$ and differentially 60% complete in the interval $R = 20.3 - 20.6$ (Geller et al. 2005; Kurtz et al. 2010).

2.1. The DLS Map (F2)

Photometric observations of F2 were made with the MOSAIC I imager (Muller et al. 1998) on the KPNO Mayall 4m telescope between November 1999 and November 2004. The R band exposures, all taken in seeing $< 0.9''$ FWHM, are the basis for the weak lensing map of F2. The total exposure is 18000 seconds; the 1σ surface brightness limit in R is $28.7 \text{ mag arcsec}^{-2}$ yielding about 45 resolved sources per square arcminute. Wittman et al. (2006) describe the reduction pipeline.

Kubo et al. (2009) carry out a maximum likelihood lensing reconstruction of F2. They

base the convergence (κ) map on sources in the range $22.0 < R < 25.5$. After removal of objects which are too small relative to the PSF, so large that they are probably nearby, or so elongated that they are probably superpositions (Wittman et al. 2006), the source catalog contains 328,000 galaxies or 23 galaxies arcmin⁻². This source density is within the range of other ground-based surveys (Miyazaki et al. 2007; Schirmer et al. 2007; Gavazzi & Soucail 2007). We use this map for our evaluation of the efficacy of the Kubo et al. (2009) weak lensing maps for locating massive clusters.

Kubo et al. (2009) construct noise maps of F2 with 100 realizations based on the source positions in the original catalog. In each realization, we assign ellipticities randomly to sources. We define σ_{DLS} as the rms deviation in the noise maps. We define the signal-to-noise as $\nu = \kappa/\sigma_{DLS}$. At each point in the image, we produce a ν map by dividing the reconstructed κ value by the rms variation in the random realizations at the same spatial positions. Kubo et al. (2009) select candidate shear peaks as local maxima in this ν map which has a pixel scale of 1.5 arcminutes/pixel.

In the F2 field of the DLS, Kubo et al. (2009) identify 12 peaks with $\nu \gtrsim 3.5$. Although Kubo et al. (2009) construct their list of potential peaks using SExtractor with a 9-pixel area filter, the peak significance for selecting the $\nu > 3.5$ peaks is determined by the signal-to-noise in the highest significance pixel. Kubo et al. (2009) also estimate a total signal-to-noise for their most significant peaks. However, their method cannot resolve overlapping peaks like those corresponding to the two massive clusters comprising Abell 781 (see Geller et al. 2005). Thus we do not use the Kubo et al. (2009) total signal-to-noise values here.

Kubo et al. (2009) tentatively identify 10 of these weak lensing peaks with plausible systems of galaxies. These cross-identifications are based on inhomogeneous data in an approach similar to Miyazaki et al. (2007) and the success rate is similar. One concern in some of these identifications (also noted by Kubo et al. (2009)) is that the separation between the center of the convergence peak and the galaxy system is as large as 4'. Schirmer et al. (2007) and Gavazzi & Soucail (2007) find that the typical separation of convergence peaks and plausibly associated galaxy systems is about an arcminute.

2.2. Lensing Sensitivity

To estimate the completeness of the weak-lensing selected cluster catalog derived from the κ map (Kubo et al. 2009), we calculate the sensitivity limits as a function of redshift. For any individual background galaxy in the weak lensing limit, the induced *measured* tangential ellipticity (and hence the S/ N for detection) depends on both the angular diameter distance

to the galaxy and on the size of the galaxy relative to the PSF. For a collection of galaxies, the effective total weight as a function of redshift is a polarizability-weighted sum over the individual distance ratios. The effective distance ratio for the ensemble of background galaxies is

$$W_{eff}(z_l) = \frac{\sum_s \frac{D_A(0, z_l) D_A(z_l, z_s)}{D_A(0, z_s)} W_s}{\sum_s W_s} \quad (1)$$

where the subscripts s and l refer to the sources and lens, respectively. W_s is the weight of each source galaxy (which depends on the object size), z_l is the lens redshift, $D_A(z_1, z_2)$ is the angular diameter distance between z_1 and z_2 , (the ratio is zero if $z_s < z_l$), and the sum is over all sources. For a realistic survey an additional suppression results from misidentification of faint foreground galaxies, each of which should have weight zero. Furthermore, in a ground-based survey, a large number of faint galaxies are unresolved. Kubo et al. (2009) reject objects with FWHM smaller than 1.2 times the PSF size; thus $W_s = 0$ for these objects.

For each redshift, we compute the angular diameter distance factors in equation (1) for each redshift assuming the “concordance” cosmology (Spergel et al. 2007). We derive the W_s terms using data from the COSMOS Subaru galaxy catalog (Taniguchi et al. 2007) and the COSMOS ACS catalog (Leauthaud et al. 2007). The COSMOS combined ACS/Subaru dataset is currently the best dataset for this calibration because it covers by far the largest area with both ground- and space-based resolution to a depth comparable to the DLS. In addition, the Subaru multi-color observations provide photometric redshift estimates (Mobasher et al. 2007) for the majority of galaxies in the survey area. We use the COSMOS catalog size and photometric redshift information to estimate the redshift distribution of the galaxies that would be resolved in DLS. The comparison of ground-based and space-based COSMOS images also provide a measure of how well resolved DLS galaxies are as a function of their DLS size. Thus the COSMOS data provide a route to a proper weighting of the DLS galaxies as a function of their probable intrinsic size in equation (1). We match galaxies in the COSMOS Subaru and ACS catalogs with the additional requirement that the catalog magnitudes in I match to within 0.3 magnitudes (This restriction eliminates errors in matching the two catalogs; it also eliminates most objects that cannot be adequately separated from neighboring objects in the Subaru imaging).

To construct a galaxy sample equivalent to the DLS sample, we select all galaxies from the COSMOS galaxy catalog with Subaru r magnitude in $20 < r < 25.3$ (a rough match to the DLS R magnitude), scale radius $> 0.3''$ (to ensure that the measured size when convolved with the DLS PSF is larger than the size cutoff in the DLS catalogs), and $0.01 < z_{phot} < 2.5$. The last cut removes some potentially catastrophic redshift errors; we

choose the high-redshift cutoff $\gg z_{max}$, the maximum lens redshift considered, to avoid biasing the high-redshift tail of the sensitivity. The cut on size produces an effective mean source redshift in the range 0.7 — 0.8. MMT spectroscopy of a small subset of the DLS sources is consistent with this estimate (Geller et al. 2005). Approximately 29,000 COSMOS objects meet all of the criteria yielding a source density comparable (but about 15% lower) with the source density of objects in the weak lensing reconstruction of DLS field F2. For each object, we compute the FWHM convolved with the mean PSF for the DLS data, and we compute the weight for that size (and PSF) as in Wittman et al. (2006). For each lens redshift, we compute W_{eff} .

Because we identify clusters from the weak lensing map based on the projected surface density within a single reconstruction pixel ($1.5' \times 1.5'$), the S/N should scale linearly with the mass enclosed within that surface area. Thus, we normalize the redshift dependence of our sensitivity by comparing to simulations. To calculate the absolute sensitivity of the weak-lensing survey to massive halos, we follow a modified version of the procedure for generating simulated catalogs in Khiabani & Dell’Antonio (2008). We generate simulated galaxies with the same size-magnitude and magnitude-redshift relations as the HDF North and South fields (Williams et al. 1996; Casertano et al. 2000) using the prescription of Khiabani & Dell’Antonio (2006). We use these simulated galaxies to populate seven logarithmically-spaced redshift shells. We then distort the images with a lens (modeled as a core-softened cutoff isothermal sphere with a given rest frame line-of-sight velocity dispersion, σ_{iso} , a $1''$ core radius, and a $100''$ cutoff radius. We resample the distorted images with the MOSAIC pixel scale, convolved with the model DLS PSF, and add noise to match the noise in the F2 image. We repeat this procedure for different values of σ_{iso} (at a fixed $z_{lens} = 0.3$) to generate maps of the weak lensing signal. We run the Kubo et al. (2009) detection method on these images to determine the value of σ_{iso} where the peak S/N reaches the $\nu = 3.5$ cluster selection limit in Kubo et al. (2009). In Figure 1, we plot the detection limit as a function of redshift ($L(z) = L(z = 0.3)W_{eff}(z = 0.3)/W_{eff}(z)$); the solid line represents $\nu = 3.5$ and the dotted lines represent the detection limits for $\nu = 3$ and $\nu = 4$, respectively. Because the detection criteria for the simulated clusters match the Kubo et al. (2009) sample, the simulation may overpredict the signal from clusters at very low redshift ($z < 0.1$); the angular region where we calculate the potential in the reconstruction encloses significantly less mass (or alternatively, we spread the same signal over multiple pixels).

There are some fundamental limitations on the accuracy of our survey sensitivity calculations. First, and most important, there is cosmic variance in the number of background galaxies behind a cluster. For clusters near the detection limit, the shear signal is detectable in a region containing only 1000-2000 galaxies; on those scales there are myriad effects that can greatly alter the number of background galaxies. Second, although the COSMOS/Subaru

field is extremely valuable, it covers $\lesssim 1$ square degree of the sky. Therefore, any systematic differences between the properties of the COSMOS field and DLS F2 can change the normalization. One of the results of the analysis of the different DLS fields is that there are strong field-to-field variations in the types and amounts of structure present on degree scales. Without large surveys, there is no way around this fundamental limitation.

There are also several more accessible sources of uncertainty in the sensitivity calibration technique. First, the computed mass sensitivity depends somewhat on the model mass profile; more centrally concentrated clusters are more easily detected. Second, because we select galaxies in the COSMOS/Subaru *r* band, which is not identical to the DLS *R* band, there is a slight bias in the redshift and size distributions of the COSMOS galaxies. Finally, the photometric redshift estimates introduce a bias if the faint galaxies have a significantly different redshift distribution from the brighter ones. However, all these sources of uncertainty change the calibration by less than $\sim 10\%$. For example, taking the magnitude cutoff in the COSMOS catalog as 24.8 instead of 25.3, a much larger change than the uncertainty in the magnitude calibration, changes the redshift of peak sensitivity by 0.01, and changes the sensitivity at $z=0.4$ by 4%. In the analysis of the incompleteness of weak lensing cluster detection, we take a 10% uncertainty in the sensitivity limit into account when determining which clusters selected from the redshift survey should be detected in the lensing map.

2.3. SHELS

We investigate the association between convergence peaks and clusters (halos) in the galaxy distribution based on a complete redshift survey. Our goal is identification of the systems of galaxies that should produce a weak lensing signal based on Figure 1. We thus identify systems in the redshift survey with rest frame line-of-sight velocity dispersion $\gtrsim 500$ km s⁻¹ (see Section 3).

We constructed the galaxy catalog from the *R*-band source list for the F2 field of the DLS. We used surface brightness to separate stars from galaxies (see Kurtz et al. 2010 for details). The final catalog contains 9825 galaxies with $R \leq 20.3$; 9603 of these galaxies have redshifts.

We acquired spectra for the objects with the Hectospec (Fabricant et al. 1998, 2005) on the MMT from April 13, 2004 to April 20, 2007. The Hectospec observation planning software (Roll et al. 1998) enables efficient acquisition of a magnitude limited sample.

The SHELS spectra cover the wavelength range 3500 — 10,000 Å with a resolution of ~ 6 Å. Exposure times ranged from 0.75 — 2 hours. The lowest surface brightness objects in the

survey required the longer integrations. We reduced the data with the standard Hectospec pipeline (Mink et al. 2007) and derived redshifts with RVSAO (Kurtz & Mink 1998) with templates constructed for this purpose (Fabricant et al. 2005). Our 1151 galaxies with repeat observations yield robust estimates of the median error in cz where z is the redshift. For emission line objects, the median error (normalized by $(1+z)$) is 27 km s^{-1} ; the median for absorption line objects (again normalized by $(1+z)$) is 37 km s^{-1} . (see also Fabricant et al. 2005).

The integral completeness of SHELS to $R = 20.3$ is 97.8%; the differential completeness at the limiting magnitude is 94.6%. The 218 objects (out of 9825) without redshifts are low surface brightness blue objects or objects near the survey corners and edges. Figure 2 shows the completeness of SHELS as a function of apparent magnitude (note that the completeness scale ranges from 0.9 to 1.0).

The SHELS survey also includes 1871 galaxies with $20.3 < R \leq 20.6$; the survey is $\sim 60\%$ complete in this magnitude interval. The completeness is patchy across the field but is generally at or above the mean in the region of the most significant weak lensing peaks.

The median redshift of SHELS is 0.295 for the magnitude limited sample with $R \leq 20.3$. Figure 3 shows the redshift distribution for the survey to a limiting $R = 20.3$. The impact of large-scale structure is obvious to a redshift $z \sim 0.55$.

3. Probing SHELS

To evaluate the correspondence between systems in the redshift survey and significant peaks in the convergence map, we develop an approach for sampling the redshift survey in narrow cones. We choose the opening angle of the cone with attention to the resolution of the weak lensing map, the density of the redshift survey in the relevant redshift range, the limitations of a magnitude limited redshift survey, the properties of massive clusters, and previous evaluations of convergence maps for cluster identification.

Our goal is to assess the *efficiency* and *completeness* of the convergence map in the identification of massive cluster halos. We define *efficiency* as the fraction of convergence map peaks with $\nu \geq 3.5$ that correspond to a SHELS cluster with a line-of-sight velocity dispersion above the solid $\nu = 3.5$ threshold curve of Figure 1. In other words, the efficiency is the fraction of weak lensing peaks that correspond to appropriately massive systems. We define *completeness* as the fraction of all clusters in SHELS with line-of-sight velocity dispersions above the threshold curve that also correspond to weak lensing peaks with $\nu \geq 3.5$. In other words, the completeness is the fraction of appropriately massive systems in SHELS that are

detected as weak lensing peaks. These definitions exclude superpositions from consideration. They also exclude coincidences between the abundant low velocity dispersion systems in the redshift survey with convergence peaks. Our definitions are similar to those adopted by Hamana et al. (2004) in their simulations of the efficacy and completeness of weak lensing surveys for massive cluster identification.

In this section, we show that sampling the redshift survey in narrow cones recovers the four known x-ray clusters with rest frame line-of-sight velocity dispersion $\gtrsim 600 \text{ km s}^{-1}$ (Section 3.1). We then use similar probes through SHELS along the lines-of-sight toward the 12 DLS convergence peaks with $\nu \geq 3.5$ and examine the presence/absence of obvious massive clusters (Section 3.2). This exercise gives us a first estimate of the *efficiency* of the convergence map for cluster detection. From SHELS we can compute a velocity dispersion for candidate systems along the line-of sight toward the most significant convergence peaks thus refining our estimate of efficiency. We also extend the investigation of the correspondence between SHELS systems and convergence peaks to $\nu \gtrsim 1$ to make a first assay of the presence of signal in the convergence map at low ν and uncover the expected increasing fraction of noise peaks with decreasing significance in the convergence map (Section 3.3). X-ray observations cover only a small fraction of F2; Section 3.4 discusses the SHELS velocity dispersions and the DLS detection/non-detection of the seven known extended cluster x-ray sources. Finally, we use SHELS as a basis for evaluating the *completeness* of the convergence map by comparing the DLS weak lensing detections with the number of clusters in SHELS that should be detected. Section 3.5 discusses the clusters in SHELS that do not appear as $\nu \geq 3.5$ peaks in the convergence map even though their optical properties indicate that they should produce a peak in the map.

3.1. Using SHELS to Evaluate Convergence Map Peaks

Schirmer et al. (2007) and Gavazzi & Soucail (2007) develop uniform procedures for evaluating the coincidence of concentrations of galaxies with convergence map peaks. Schirmer et al. (2007) compare the galaxy counts with $R \sim 17\text{--}22$ in a cone of $2'$ radius centered on a lensing peak with the galaxy density in the surrounding field. They assign significance classes to the excess counts based on Poisson statistics. Gavazzi & Soucail use the distribution of photometric redshifts for galaxies brighter than $i' = 23$ in $2'$ radius probes. They subtract a background photometric redshift distribution from each of the probes. They then compute the background from the survey area more than $6'$ from any peak.

The approaches of both Schirmer et al. (2007) and Gavazzi & Soucail (2007) are based on complete photometric surveys of their fields. They evaluate the significance of cluster

candidates internal to their surveys.

We follow a similar approach with a complete redshift survey. Because the redshift survey is complete we can sample the survey itself to evaluate the significance of galaxy condensations along the line-of-sight to lensing peaks. The redshift survey is shallower than the corresponding photometric surveys. We demonstrate below that redshifts for the more luminous galaxies in condensations at redshifts from 0.2–0.53 are adequate to demonstrate correspondence (or lack of it) between the weak lensing peaks and clusters of galaxies in the redshift survey. We briefly explore the dilution of a “cluster” signal in photometric redshift data in Section 5. The sensitivity plot (Figure 1) suggests that we need not look deeper than $z \sim 0.55$ to identify clusters corresponding to the weak lensing peaks; more distant systems must be very rich and they should be obvious in the photometric data. Kubo et al. (2009) find no evidence for such higher redshift systems.

Probes through the redshift survey centered on each galaxy in the survey contain all of the selection effects which impact a probe toward a lensing peak. Thus comparison of these probes with similar probes toward the peaks should provide a robust measure of the significance of cluster candidates in the redshift survey. We have demonstrated by experiment that centering of probes on galaxies or on random points in the region has no effect on the results of our analysis.

The steps in our candidate cluster identification procedure are:

1. We sample the SHELS survey complete to $R = 20.3$ in *test cones* with $3'$ radius centered on each galaxy in the complete redshift survey. The cones are large enough to detect a galaxy cluster across the redshift range we sample.
2. In each *test cone* we count the number of additional galaxies, N_{gal} , within a bin of $1600(1+z)$ km s^{-1} centered on the survey galaxy. The bin size is comparable with the extent in redshift space of systems we wish to identify. The bin width is conservatively large.
3. In each of the redshift bins of item 2, we evaluate the mean occupation and the variance (σ_{SH}) across the entire survey. We then identify the set of *test cones* at each redshift which are $5\sigma_{SH}$ above the mean occupation and contain at least 6 galaxies ($N_{gal} \geq 5$). The minimum number of galaxies enables computation of a dispersion (albeit with large error). The $5\sigma_{SH}$ limit restricts the sample to high peaks which are reasonable candidate clusters especially at the peak sensitivity of the survey, $z \sim 0.3$. Both the 6 galaxy and $5\sigma_{SH}$ limits are generous; they admit many peaks well below the expected detection threshold for the weak lensing map (Figure 1). We call these probes *$5\sigma_{SH}$ probes* hereafter.

Figure 4 shows a map of the F2 region. Each gray point marks the position of a galaxy at the center of a $5\sigma_{SH}$ probe. As a basic test of the efficacy of these probes in identifying known clusters of galaxies, the open circles in Figure 4 show that the locations of four known x-ray clusters, XMMU J091935+303155, CXOU J092026302938, CXOU J092053+302900, and CXOU J092110+302751, coincide with highly ranked probes. The cluster XMMU J091935+303155 is undersampled in the redshift survey because a saturated bright star ($R \lesssim 18$) is superposed near its center. We comment further on these clusters in Section 3.4.

Kubo et al. (2009) find 12 peaks in the convergence map with signal-to-noise $\nu \geq 3.5$. The numbers in Figure 4 are centered on the coordinates of these significant weak lensing peaks. Table 1 of Kubo et al. (2009) lists the coordinates and value of ν for these peaks. The significance of these peaks is similar to the peaks considered in other convergence maps and in the simulations by Hamana et al. (2004).

In Figure 4 the two most significant weak lensing peaks are coincident with the two x-ray clusters, CXOU J092026+302938 and CXOU J092053+302900. These two clusters coincide with the cluster A781. All of the weak lensing peaks except 4, 6, 8 and 12 lie within $3'$ of the center of at least one well-populated probe.

There are obviously many well populated probes without any associated significant weak lensing peak. Many of the well-populated SHELS probes correspond to groups at a redshift $\lesssim 0.3$. From Figure 1 we would not expect these systems with $\sigma_{los} \lesssim 500 \text{ km s}^{-1}$ to produce a significant signal in the κ map.

To further assess the meaning of the weak lensing peaks we examine the redshift distributions along the line-of-sight toward each of the significant peaks. We ask which lines-of-sight intersect a cluster with a velocity dispersion large enough to plausibly account for the weak lensing peak (Section 3.3). We also investigate the coincidence of SHELS systems with lower significance convergence peaks with $1 < \nu < 3.5$ (Section 3.3). Finally, we check all of the $5\sigma_{SH}$ peaks in Figure 4 to see whether any others contain systems with large enough velocity dispersion that they should be detected according to the sensitivity plot (Figure 1; Section 3.5). We can then evaluate the completeness of the DLS cluster detections (see Sections 4 and 6).

3.2. Convergence Map Peaks and Candidate Galaxy Systems

In this section we evaluate candidate systems along the line-of-sight toward weak lensing peaks. We begin with the 12 most significant DLS peaks. We extend the discussion to all

DLS peaks with $\nu \gtrsim 1$ in Section 3.5.

Figures 5, 6, 7, and 8 show the redshift, z , distributions of galaxies within $3'$ probes centered on each of the 12 highest significance DLS peaks (see Figure 4). The bins are $800(1+z)$ km s $^{-1}$. The dark histogram shows galaxies with $R \leq 20.3$; the gray histogram shows galaxies with $R \leq 20.6$. The histograms fall in three categories: (1) there is an obvious single peak which probably corresponds to a system of galaxies (2) there is more than one apparently significant peak, and (3) there are no significant peaks.

The probes toward peaks 1, 2, and 5 each contain an impressive peak. These peaks correspond to clusters of galaxies; we evaluate the dispersions in Section 3.3.

Peak 3 contains several well-populated peaks at redshifts 0.28 — 0.34. Peaks 4, 6, 8, and 12 contain no well-populated peaks. If there are condensations in redshift space near these peaks, most of the galaxies are more than $3'$ from the position of the weak lensing peak. With a larger search radius of $4'$, Kubo et al. (2009) identify candidate systems associated with convergence map peaks 8 and 12.

Figure 9 shows higher resolution histograms for weak lensing peaks 3 and 5 in both $3'$ and $6'$ probes. The upper histograms show the distributions for the magnitude limited samples with $R \leq 20.3$; the lower histograms show all of the galaxies with $R \leq 20.6$. The difference in the redshift distributions is obvious particularly in the better sampled histograms. Peak 5 is a cluster with a rest frame velocity dispersion of 729 ± 41 km s $^{-1}$ ($3'$ probe); the line of sight toward peak 3 contains a superposition of three peaks with rest frame velocity dispersions of 150, 260, and 340 km s $^{-1}$.

A detailed model is necessary to assess whether the superposed low mass systems along the line-of-sight toward peak 3 can account for the weak lensing signal. This detailed discussion is beyond the scope of this paper; for the rest of the discussion we focus on lines-of-sight which include a plausibly rich cluster. We concentrate on evaluating the weak lensing map as a method of identifying these rich systems.

The lines-of-sight toward peaks 7 and 9 each contain a peak populated by ~ 10 galaxies. Peak 10 has a peak at 0.185 along with a peak at 0.53. The redshift survey is sparse at $z \sim 0.5$; thus the number of galaxies in the peak at 0.53 is still indicative of the presence of a system (see Section 3.3). The fainter galaxies obviously enhance the peak. The situation is similar for the line-of-sight toward peak 11; there is a peak at $z = 0.53$ again enhanced by the fainter galaxies (see Section 3.4).

The apparent systems which appear as peaks in the redshift survey have a large range in velocity dispersion. We next determine which of these peaks correspond to systems with

velocity dispersion (mass) sufficient to account for the weak lensing signal.

3.3. Velocity Dispersions of Weak Lensing/SHELS Candidate Systems

In this section we compute velocity dispersions for systems within our $3'$ probes. To construct a complete catalog of massive systems which should be detected by the DLS at $\nu \geq 3.5$, we consider all apparent systems with rest frame line-of sight velocity dispersion $\sigma_{los,3} \gtrsim 500 \text{ km s}^{-1}$ measured from the $R \leq 20.3$ catalog. The velocity dispersion limit lies significantly below the $\nu = 3.5$ threshold in Figure 1. We also examine weak lensing peaks with statistical significance $\nu \gtrsim 1$ to examine the overall signal in the weak lensing map and to evaluate the frequency of accidental superpositions between weak lensing peaks and clusters in SHELS.

We use SHELS redshifts for galaxies with $R \leq 20.6$ to compute the rest frame velocity dispersion, $\sigma_{los,3}$, for each of the candidate systems within a $3'$ probe centered on the position of the weak lensing peak. We also compute the rest frame velocity dispersion for each candidate system within a $6'$ probe concentric with the $3'$ probe. We make this comparison because the determination of the velocity dispersion of the clusters which comprise the A781 complex is problematic as a result of system overlap in redshift space. In general, the comparison of these two apertures also gives a measure of the systematic error in the determination of the velocity dispersion.

Table 1 lists the candidate systems and their properties for both a $3'$ and a $6'$ radius centered at the listed RA_{2000} (column 4) and DEC_{2000} (column 5). The Table includes systems along the line-of sight toward weak lensing peaks with $\nu > 1$ as well as candidate SHELS systems where there is no corresponding peak in the convergence map. Table 1 lists the candidate cluster name (column 1), the rank of the corresponding DLS peak if there is one (column 2), the ν of the weak lensing peak (column 3), the mean redshift of the SHELS candidate system (column 5), the rest frame line-of-sight velocity dispersion within the $3'$ radius, $\sigma_{los,3}$ (column 7), the number of survey galaxies in the $3'$ system, N_3 (column 8), the bootstrap error in $\sigma_{los,3}$, err_3 (column 9), the rest frame line-of-sight velocity dispersion within the $6'$ radius, $\sigma_{los,6}$ (column 10), the number of survey galaxies in the $6'$ system, N_6 (column 11), and the bootstrap error in $\sigma_{los,6}$, err_6 (column 12). For weak lensing peaks 1 and 2, the Table lists only $6'$ quantities. We discuss this issue in detail below. In all other cases we limit the range where we compute the velocity dispersion with standard 3σ clipping. For nearly all of the cluster candidates (regardless of a counterpart in the weak lensing map), the rest frame velocity dispersions in the two apertures differ by $\lesssim 2\sigma$. In fact, the only exception is DLS peak 15 where the difference is 2.2σ .

The abundance of systems of galaxies increases steeply with decreasing line-of-sight velocity dispersion. We limit our discussion of candidate lensing systems to massive halos with $\sigma_{los,3} \gtrsim 500 \text{ km s}^{-1}$. Coincidences of weak lensing peaks with individual much less massive systems are common, as are superpositions along the line-of-sight. Of course, the greater abundance of these systems implies a larger chance of mismatching halos with weak lensing peaks (see Hamana et al. (2004)). Analysis of this issue is beyond the scope of this paper.

For the range of candidate cluster redshifts in Table 1, the $3'$ radius corresponds to 0.38 Mpc ($z = 0.12$) and to 1.1 Mpc ($z = 0.53$). These radii are within r_{200} , the radius where the enclosed average mass density, $\rho(< r)_{200} = 200\rho_c$. Here ρ_c is the critical density. The radius r_{200} , a proxy for the virial radius, ranges from 1.0 to 2.0 Mpc for well-sampled clusters with rest frame line-of-sight velocity dispersions in the range 500 km s^{-1} to 1000 km s^{-1} (Rines et al. 2003; Rines & Diaferio (2006). According to the scaling relations of Rines & Diaferio (2006), the corresponding range of masses, M_{200} , within r_{200} is $1.2 \times 10^{14} M_\odot$ to $1.2 \times 10^{15} M_\odot$.

Rines & Diaferio (2006) show that the velocity dispersion in a cluster decreases with radius. For clusters at larger redshift the tendency to underestimate the velocity dispersion in our physically larger aperture is compensated by the increasing difficulty of eliminating velocity outliers in the sparser samples.

Determination of the central velocity dispersion for weak lensing peaks 1 and 2 is problematic because they overlap substantially in redshift space. Geller et al. (2005) published rest frame velocity dispersions of $741^{+35}_{-40} \text{ km s}^{-1}$ and $674^{+43}_{-52} \text{ km s}^{-1}$ for peaks 1 and 2, respectively, based on identification of cluster members in a friends-of-friends group finding algorithm applied to less complete SHELS data. Here we explored the region of the A781 complex by first assessing the global redshift distribution within a $30'$ region centered midway between the coordinates listed in Table 1 for these systems. There are two well-defined peaks centered at redshifts 0.2915 (peak 1) and 0.3004 (peak 2) in essential agreement with the mean redshifts for these systems in Geller et al. (2005). Application of the routine *mrqmin* (Press et al. 1992) returns velocity dispersions for peaks 1 and 2 that substantially underestimate the central velocity dispersions because they sample well into the cluster infall region (Rines et al. 2003; Rines & Diaferio 2006). The mean redshifts are, however, robust and we use them to compute the velocity dispersion in the central regions of the clusters.

To estimate the central rest frame velocity dispersion of peaks 1 and 2, we fix the mean redshift at the values obtained for the global sample (Table 1). For samples within a $3'$ radius of each center, a fit of two Gaussians in the Press et al. (1992) routines does not converge. Within a $6'$ radius (a physical radius of $\sim 1.5 \text{ Mpc}$, roughly the expected r_{200} for these clusters) around each of the two centers, the fits converge to the rest frame dispersions

in Table 1. The error in Table 1 is an approximate and conservative estimate; the errors are dominated by systematic issues in separating the two clusters in redshift space. This approach yields systematically larger velocity dispersions than the group-finding algorithm used in Geller et al. (2005), but the differences are within the large error. Regardless of the method of assessing the velocity dispersion of these clusters, they both exceed the $\nu = 3.5$ threshold (Figure 1).

There are 10 SHELS candidate systems along the line-of-sight toward weak lensing peaks with $\nu > 1$. In one case, weak lensing peak 10, there are two systems along the line-of sight, one at $z = 0.18$ along with a more massive system at $z = 0.53$. The median separation between the lensing peak positions and the centers of the candidate galaxy cluster is $0.5'$ in agreement with the similarly small separations found in previous surveys (Gavazzi & Soucail 2007; Schirmer et al. 2007). Figure 10 shows the DLS weak lensing peak rank as a function of statistical significance.

Solid dots in Figure 10 represent cases where SHELS reveals a cluster along the line-of-sight to the peak with a rest frame velocity dispersion $\gtrsim 500 \text{ km s}^{-1}$ and $z < 0.55$. It is interesting to note that, as expected, the fraction of “cluster detections” (solid dots) is larger for $\nu_{DLS} \geq 3.5$ than at lower significance. In Section 4 we estimate the accidental coincidence rate and show that there is some signal in the weak lensing map at $\nu_{DLS} < 3.5$ even though, as expected, it is diluted by an increasing abundance of noise peaks as ν_{DLS} decreases. In contrast with Kubo et al. (2009), we find only 4 (rather than 10) convincing coincidences between rich clusters and weak lensing peaks with $\nu \geq 3.5$. The main reasons for the difference between our results and Kubo et al. (2009) are (1) our use of the redshift survey to compute line-of-sight velocity dispersions and (2) our use of a smaller search radius (consistent with the small offsets between lensing peak positions and galaxy system centers observed by other investigators from both data and simulations). Kubo et al. (2009) count superpositions like peak 3 as weak lensing detections; we count only candidate systems which have a large enough SHELS line-of-sight velocity dispersion to exceed the $\nu = 3.5$ threshold. We conclude that the weak lensing detection efficiency for $\nu \geq 3.5$ is 33%.

3.4. Known X-ray Clusters in the DLS Field

Chandra and XMM observations cover 14% of the DLS field with widely variable sensitivity. As a result of these observations there are seven known extended cluster x-ray sources in the field (Figure 11). Both Chandra and XMM observations target the region near A781 which, remarkably, contains 4 cluster x-ray sources (Table 2 and Figure 11). In order of right ascension, Table 2 lists the x-ray cluster name (column1), the rank of any corresponding DLS

peak (column 2), the RA_{2000} and DEC_{2000} (columns 3 and 4), the rest frame line-of-sight velocity dispersion determined from the SHELS galaxies in the system with $R < 20.6$ in a $3'$ cone (except for CXOU J092026+302938 and CXOU J092053+302900 where we quote the $6'$ dispersions from Table 1) centered on the x-ray position (column 5), the number of galaxies in the system (column 6) the bootstrap error in the velocity dispersion (column 7), and the *Chandra* x-ray flux from the literature (column 8). Double line entries for a single x-ray system indicate superposed structure in SHELS along the line-of-sight.

The two clusters CXOU J092026+302938 and CXOU J092053+302900 are at redshifts of 0.3004 and 0.2915 respectively; these two clusters correspond to the original A781. They are also responsible for the two most significant weak lensing peaks in the Kubo et al. (2009) map. The cluster CXOU J092026+302938 is complex; CXOU J092053+302900 is a simpler system (Wittman et al. 2006; Sehgal et al. 2008).

Khiabanian & Dell’Antonio (2008) developed the lensing map reconstruction technique applied by Kubo et al. (2009). In addition to the map with a uniform $1.5'$ resolution, Khiabanian & Dell’Antonio (2008) show a map with a resolution of $0.9'$ in the regions around A781. This map reveals a detection of a third x-ray cluster CXOU J092026+302938 and CXOU J092053+302900 with a $S/N \sim 5.7$. SHELS shows that this cluster has a mean redshift of 0.43 and a velocity dispersion of $754 \pm 92 \text{ km s}^{-1}$ (Table 2).

The fourth extended cluster x-ray source in the region of A781, XMMU J091935+303155, is a puzzling and complex case. There is a well-defined, blue arc associated with the first-ranked galaxy located at $RA_{2000} = 9:19:35.063$, $DEC_{2000} = 30:31:56.627$, very close to the x-ray center. Our attempt to measure a redshift for the arc with the Blue Channel spectrograph on the MMT resulted in detection of a blue continuum but no emission lines. Thus the redshift of the arc is probably $\gtrsim 1.2$. The mean cluster redshift, 0.43, is essentially the same as the redshift of the first-ranked galaxy (0.4276). This cluster is undersampled in SHELS because a region very close to the cluster center is excised around saturated bright star ($R \lesssim 18$).

Although the velocity dispersion and redshift of XMMU J091935+303155 should put it above the detection threshold for the weak lensing map, there is no significant peak associated with this system. The XMM observations (Table 6 of Sehgal et al. (2008)) show that XMMU J091935+303155 has about twice the x-ray flux and nearly the same temperature as CXOU J092110+302751. CXOU J092110+302751 is at the same redshift and is cleanly detected in the higher resolution DLS weak lensing map (Khiabanian & Dell’Antonio 2008). In contrast, we find only a $\nu = 0.5$ enhancement in the convergence map at the position of XMMU J091935+303155. Sehgal et al. (2008) make an *a posteriori* model fit to the convergence map based on the x-ray data and argue for a weak detection. Both the SHELS data and the

XMM observations suggest that the cluster should appear at a $\nu > 3.5$ in the convergence map.

In separate deep imaging with Chandra, Wittman et al. (2006) discovered three more extended x-ray sources: CXOU J091551+293637, CXOU J091554+293316, and CXOU J091601 +292750 (see Table 2 and Figure 11). In Figure 4, possible optical counterparts of CXOU J091551+293637 and CXOU J091554+293316 appear as populated $5\sigma_{SH}$ probes. CXOU J091551+293637 and CXOU J091554+293316 are adjacent to weak lensing peak 11 and 8 respectively. These systems do not appear in Table 1 because the velocity dispersion for samples centered on the weak lensing peaks and/or for samples limited to $R < 20.3$ fail our minimum cut of 500 km s^{-1} .

Table 2 lists line-of-sight velocity dispersions for condensations of galaxies along the line-of-sight toward these three extended x-ray sources. For CXOU J091551+293637, the probable first-ranked galaxy in the x-ray emitting system is within $30''$ of the x-ray center and has a redshift of 0.53. We thus identify the extended x-ray source as a rich group at $z = 0.53$ with a rest frame line-of-sight velocity dispersion of $360 \pm 70 \text{ km s}^{-1}$. The first-ranked galaxy and the ten other probable members of the system are all fainter than $R = 20.3$. Thus foreground structure at $z \sim 0.18$ is responsible for the $5\sigma_{SH}$ probes in Figure 4. In Table 2 we quote a velocity dispersion for this foreground structure that is merely the spread of redshifts within the large-scale structure intercepted by our probe.

The x-ray source CXOU J091554+293316 has the lowest flux of the three (Wittman et al. 2006). There is no convincing optical counterpart; the nearest galaxy is an arcminute away from the x-ray center and only 7 other galaxies within our $3'$ probe appear clustered at the $z = 0.18$; a normal x-ray emitting group at this redshift should be easily detectable with many members in a deep survey like SHELS. We list an apparent velocity dispersion in Table 2, but this dispersion is again a measure of the spread of redshifts within the large-scale structure intercepted by our probe.

The center of the southernmost extended x-ray source, CXOU J091601+292750, is within $10''$ of a galaxy at $z = 0.53$. An additional six galaxies at similar redshift yield an estimate of the rest frame line-of-sight velocity dispersion for this system of $523 \pm 71 \text{ km s}^{-1}$. The foreground structure seen in the lines of sight toward CXOU J091551+293637 and CXOU J091554+293316 is also present here. Again the velocity dispersion for this structure at $z = 0.18$ is indicative of the spread of redshifts within the foreground large-scale structure. There is no weak lensing peak near this x-ray system.

The rest frame velocity dispersions for all three systems (CXOU J091551+293637, CXOU J091554+293316, and CXOU J091601+292750) should place them below the $\nu = 3.5$

detection threshold for the weak lensing map (Figure 1). Kubo et al. (2009), however, associate these clusters with weak lensing peaks 8 and 11. It is conceivable that foreground structure at $z = 0.18$ and overlap among the clusters boosts the weak lensing signal; detailed modeling beyond the scope of this paper is necessary to understand whether these superpositions are adequate to explain the apparent weak lensing detection.

Among the seven known x-ray clusters in the DLS fields, only three (CXOU J092026+302938, CXOU J092053+302900 and CXOU J092110+302751) are cleanly detected as peaks with $\nu > 3.5$ in the convergence map provided the resolution is adequate. The cluster XMMU J091935+303155, detected by XMM and SHELS but not by the DLS, is puzzling. Another 3 clusters at greater redshift (and lower rest frame velocity dispersion) may be detected in the DLS map as a complex superposition; the SHELS velocity dispersions and the sensitivity curve for the convergence map suggest that none of these systems should be detected on their own.

This analysis of x-ray observations of a small portion of the DLS field demonstrates some problematic issues for construction of catalogs of clusters of galaxies from weak lensing maps: (1) coarse resolution of the weak lensing map dictated by the density of sources can reduce the number of clusters in an uncontrolled way, (2) superpositions may increase the number of apparent detections in a complex way, and (3) inconsistencies among different cluster detection methods need to be understood both from simulations and from larger observational samples where direct comparison is possible. Bergé et al. (2008) are, for example, undertaking such an observational project in the x-ray.

3.5. SHELS Cluster Candidates

SHELS obviously enables identification of cluster candidates independent of the weak lensing map. There are many reasonable approaches to the identification of candidates. For consistency, we use the 3' probes of Figure 4. Other algorithms including the identification of systems with a friends-of-friends algorithm yields very similar results for these dense, well-populated systems (Ramella et al. 2010).

To construct a catalog of cluster candidates for $z < 0.55$ we start with the probes shown in the map of Figure 4. We first identify all probes with at least 6 galaxies with $R \leq 20.3$ (significance $\gtrsim 5\sigma_{SH}$) in any redshift interval, $1600(1+z)$ km s⁻¹, and with apparent velocity dispersion $\gtrsim 500$ km s⁻¹. We then examine all overlapping probes and choose the most populated to represent the system. We choose the center of this probe as the indicative center of the system.

The probes in Figure 4 are based solely on galaxies with $R < 20.3$. We next include the additional galaxies with $20.3 < R \leq 20.6$. The broad window we use to construct the map may admit several groups with small velocity dispersion as in Peak 3. Increased sampling enables elimination of several systems where we can identify better defined multiple peaks as convincing superpositions. We list all of the SHELS cluster candidates in Table 1. For completeness we include all of the candidate clusters we find with line-of-sight velocity dispersion $\gtrsim 500 \text{ km s}^{-1}$ even though many of these should not be detected at high significance in the DLS weak lensing map. For redshifts $\lesssim 0.4$ we easily identify clusters with line-of-sight velocity dispersion $\sim 500 \text{ km s}^{-1}$; for larger redshift the lowest velocity dispersion system has $\sigma_{los,6} = 642 + / - 70 \text{ km s}^{-1}$.

The sample of SHELS candidate clusters with velocity dispersions large enough to be detected in the DLS weak lensing map should be complete (see Figure 1). The set of 20 SHELS clusters (Table 1) includes 10 systems along the line-of-sight toward weak lensing peaks with $\nu \gtrsim 1$. We also find the two additional x-ray clusters SHELS J0921.2+3028 (CXOU J092110+302751) and SHELS J0919.6+3032 (XMMU J091935+303155). A higher resolution weak lensing map detects the first of these; there is no weak lensing detection of the second (see Section 3.4). Considering the errors in the line-of-sight velocity dispersion, $\sigma_{los,6}$, the SHELS candidate cluster list includes eight clusters with line-of-sight velocity dispersion large enough that they should be detected with $\nu \gtrsim 3.5$ in the DLS map at the resolution we explore here; only four of them are detected (we exclude J0921.2+3028 which requires a higher resolution map for DLS detection). All four of the undetected clusters are at a redshift $z \sim 0.4$. It is interesting that three of these clusters (two at $z \sim 0.4$) are along the line-of-sight toward DLS peaks with $1.6 \leq \nu < 2.9$. Details of the cluster structure, voids along the line-of-sight, and noise in the κ map may all contribute to reduction of the weak lensing signal (Hamana et al. 2004). Our data do not allow discrimination among these possibilities.

4. Weak Lensing and Cluster Detection

Figure 12 summarizes the joint detection of systems in the DLS and in SHELS. Each of the symbols represent one of the 20 SHELS candidate clusters in Table 1. The solid curve shows the expected $\nu = 3.5$ detection threshold in the DLS. Figure 12 indicates sensitivities of $\nu = 3$ (lower dotted curve) and $\nu = 4$ (upper dotted curve). We use $\sigma_{los,6}$ for uniformity across the SHELS sample.

The four filled triangles indicate the SHELS clusters coincident with DLS $\nu \geq 3.5$ peaks. Note that clusters at $z = 0.1844$ and $z = 0.5343$ are superposed along the line-of-sight toward

DLS peak 10; we show the superposed lower redshift system as an open triangle. Among the top 12 DLS peaks there are 4 detections of clusters of galaxies (peaks 1, 2, 5 and 10). Peaks 3, 8, and 11 may reflect lensing signal from superpositions (see Sections 3.2 and 3.4). Conservatively, the efficiency of cluster detection is 33% for weak $\nu \geq 3.5$ weak lensing peaks. The efficiency for the 7 $\nu \geq 4$ peaks increases to 43%.

The filled star in Figure 12 corresponds to the x-ray cluster SHELS J0916.2+2949 CXOU J092110+302751. In the regions around A781, Khiabanian & Dell’Antonio (2008) construct a higher resolution map which has a $\nu \sim 5.7$ peak coincident with this cluster. Wittman et al. (2006) also identify it in their higher resolution weak lensing map of F2.

The five open squares correspond to weak lensing peaks with $1 \leq \nu < 3.5$ and with a SHELS cluster along the line-of-sight. If the weak lensing peaks were uncorrelated with systems of galaxies we would expect 2.5 ± 0.5 of the 63 weak lensing peaks would fall within the 20 $3'$ probes where we identify clusters in SHELS. This estimate of chance coincidences is probably overly generous because the median separation between the center of a SHELS cluster and a weak lensing peak is only $0.5'$ with a maximum separation of $1.5'$. If we require that the centers of the weak lensing peaks and the SHELS clusters be less than $1.5'$, the expected number of accidental coincidences obviously drops by a factor of 4 to 0.6 ± 0.1 , a negligible contamination. We conclude that there is signal in the weak peaks at $\nu < 3.5$; the coincidences between SHELS clusters and lower significance DLS lensing peaks are probably not accidental. As expected the efficiency of halo detection decreases with the significance of the weak lensing peaks. Of course, the clusters in the DLS field are embedded in the large-scale structure and contribute to the cross-correlation signal Geller et al. (2005) find between the DLS convergence map and a velocity dispersion map constructed from SHELS.

The 9 open circles are candidate clusters in SHELS with no corresponding DLS peak at significance $\nu \gtrsim 1$. Again the five open squares represent candidate SHELS clusters along the line-of-sight toward DLS peaks with significance $1 \leq \nu < 3.5$. Among these systems indicated by open squares and circles, four should be detected by the DLS at $\nu \geq 3.5$; two of these systems (open squares) are along the line-of-sight toward lower significance weak lensing peaks. Thus the completeness of the DLS cluster detection (the fraction of SHELS clusters with velocity dispersions above the $\nu = 3.5$ threshold detected by the DLS) is $\sim 50\%$. This completeness level is similar to the one predicted by the simulations of Hamana et al. (2004): we discuss this similarity further in Section 6.

Figures 12, 13, and 14 show DLS images of the central $6' \times 6'$ of each of the nine clusters in SHELS with rest frame line-of-sight velocity dispersion measurements placing them about the DLS $\nu = 3.5$ threshold. Among these clusters SHELS J0920.9+3029 and SHELS J0920.4+3030 (they are coincident with A781 at $z \sim 0.3$) and SHELS J0916.2+2949

at $z \sim 0.5$ are obviously very rich systems. Among the five clusters at $z \sim 0.4$, there is no obvious optical property that should discriminate between weak lensing detection and non-detection. At $z \sim 0.3$, the peak sensitivity of both SHELS and the DLS, all three clusters within SHELS which should be detected in the DLS map at $\nu \geq 3.5$ correspond to significant weak lensing peaks. The situation at greater redshift is puzzling. Clusters detected as weak lensing peaks and those undetected have the same rest frame line-of-sight velocity dispersions within the errors. For the clusters at $z \sim 0.4$ the number of galaxies within SHELS for the detected cluster is about twice the number in the undetected ones. These variations in population are unlikely to explain the weak lensing non-detections; variations of a factor of two at a fixed cluster mass (velocity dispersion) are typical of the cluster population at lower redshift (see e.g. Lin et al. 2004).

Even for peaks in the weak lensing map with significance $\nu \geq 3.5$, cluster detection is neither complete nor efficient (Hamana et al (2004); Hennawi & Spergel (2005)). The weak lensing map is $\sim 50\%$ complete relative to the catalog derived from the SHELS survey. Among the 12 DLS peaks with high significance, only 33% are associated with massive clusters. Admittedly the sample of significant weak lensing peaks is small, but the comparison with SHELS suggests that observational assessments of weak lensing maps based on counts along the line-of-sight and/or on photometric redshifts may lead to overly optimistic assessments of weak lensing as a tool for the construction of catalogs of massive systems in the universe.

5. Degrading SHELS Redshifts — A Perfect Photo z Model

Previous techniques for identifying candidate systems corresponding to convergence map peaks include the use of galaxy counts, photometric redshifts, and x-ray images. In the largest datasets to date, the efficiency of cluster detection ranges from 45% (Schirmer et al. 2007) to 80% (Miyazaki et al. 2007).

In this section we focus on the use of photometric redshifts and demonstrate by example that this approach can easily fail to discriminate between a superposition along the line-of-sight and a massive cluster. Although some superpositions are so widely separated in redshift that one could weed them out with photometric redshifts, a large fraction are so close together that photometric redshifts are a useless discriminant. We degrade the SHELS redshift survey to produce a “perfect” set of 3% photometric redshifts. We then examine weak lensing peaks ranked 3 (a superposition; Figure 9) and 5 (a cluster at $z = 0.3$; Figure 9) as an example of the impact of photometric redshifts of typical accuracy on the assessment of cluster detection.

Typical photometric redshifts for luminous red galaxies are accurate to $\Delta z/(1+z) \sim 0.03$ (Padmanabhan et al. 2005; Kurtz et al. 2007). To simulate the result of a photometric redshift survey of F2 to the same depth as SHELS we simply replace the redshift for each galaxy with a photometric redshift drawn from a Gaussian distribution with a dispersion of $0.03(1+z)$. Obviously these photometric redshifts are perfect; we do not simulate the impact of systematic error and we ignore the difficulty of obtaining accurate photometric redshifts for bluer objects.

As a telling example of the impact of photometric redshifts, we revisit weak lensing peaks 3 and 5 (Figure 9). Figure 16 again shows the SHELS redshift distribution for peaks 3 and 5, but here we focus on the redshift range 0.2 to 0.4 (panels labeled Peak 3 and Peak 5). The bins are 250 km s^{-1} . The difference between the superposition along the peak 3 line-of-sight and the cluster along the peak 5 line-of-sight is obvious. Companion panels show the simulated 3% photometric redshift distribution along the lines-of-sight toward peaks 3 and 5. The two redshift distributions with perfect photometric redshifts are nearly indistinguishable. There are 111 galaxies with $R < 20.6$ in the redshift interval for Peak 3; there are 86 for Peak 5. Thus the distribution of simulated photometric redshifts for peak 3 appears somewhat more impressive even though the galaxies lie in concentrations with smaller velocity dispersion ($150 - 340 \text{ km s}^{-1}$) than the cluster along the line-of-sight toward peak 5 (729 km s^{-1}).

Photometric redshifts dilute real clusters and make superpositions look like clusters if the redshift range covered by the superposition is comparable with or less than the accuracy of the photometric redshifts. Because the uncertainty in a photometric redshift is large compared to the velocity dispersion of a cluster (or to the scale of voids in a redshift survey), the resulting distribution of photometric redshifts indicates the number of galaxies in a redshift range rather than the more physical quantity, the velocity dispersion of a system or systems of galaxies. We conclude that the use of photometric redshifts compromises the distinction between clusters and superpositions of several lesser systems along the line-of-sight. Thus, without spectroscopic redshifts, an excessive number of weak lensing peaks appear to correspond to “clusters”.

6. Discussion

Combining the SHELS redshift survey with the DLS weak lensing map provides an assessment of both the efficiency and completeness of weak lensing in identifying massive clusters. As demonstrated by the theoretical models of Hamana et al. (2004), the efficiency and completeness of a catalog of massive clusters derived from weak lensing are a strong

function of the cutoff S/N used to identify peaks in the weak lensing map. Maturi et al. (2009) add further weight to this conclusion. Hamana et al. (2004) and Maturi et al. (2009) conclude that minimum S/N cutoffs in the range 3-5 give an optimal balance between completeness and efficiency. Both Hamana et al (2004) and Hennawi & Spergel (2005) show that there are intrinsic limitations, independent of observational issues, in both the efficiency of weak lensing cluster identification and in the completeness of cluster catalogs derived from weak lensing.

Dietrich et al. (2008) also use ray-tracing simulations to gain understanding of the efficacy of convergence maps for massive halo detection. They calculate the cumulative distribution of offsets between the positions of peaks in the convergence map and the centers of massive halos. They show that 75% of the offsets are less than $2.15'$. This offset is larger than the typical offset we find between peaks in the DLS map and SHELS systems: we find a mean offset of $0.5'$ and a maximum of $1.5'$. The redshift range of the SHELS clusters coincident with DLS peaks is similar to the range considered by Dietrich et al. (2008), but different weighting with redshift may contribute to the difference in offsets.

Comparison of the catalog of systems with $\sigma \gtrsim 500 \text{ km s}^{-1}$ derived from SHELS with the significant peaks in the DLS map provides estimates of *both* the efficiency and completeness of the set of systems detected in the weak lensing map. To our knowledge this comparison extending to low significance weak lensing peaks is the first of its kind. We can compare the measures of efficiency and completeness with the ray-tracing simulations of Hamana et al. (2004). We can also compare the completeness of weak lensing detections as a function of redshift. Next, we briefly review the conclusions of Hamana et al. (2004) and compare them with our results.

Hamana et al. (2004) used analytic calculations and ray-tracing through large n-body simulations to explore the effectiveness of weak lensing surveys in identifying massive clusters of galaxies. They show that $\nu \gtrsim 4$ gives an optimal balance between efficiency and completeness in cluster identification. Their fiducial survey has $\sim 30 \text{ sources arcmin}^{-2}$ with the typical source as $z \sim 1$ in contrast with the DLS source density of $23 \text{ sources arcmin}^{-2}$ and typical source redshift of $0.7 - 0.8$. In simulated weak lensing maps with noise properties similar to the observations, Hamana et al. (2004) calculate that the completeness is $\sim 63\%$ and the efficiency is $\sim 37\%$ for $\nu > 4$. These statistics apply only to clusters which should be detected at or above the weak lensing threshold. They omit clusters which should appear below the threshold but are boosted by noise. This boosting increases the apparent efficiency by $\sim 20\%$. Hamana et al. (2004) emphasize the fascinating and surprising result that noisy maps boost the completeness of cluster detection at the expense of efficiency (Figure 16 of their paper).

We can use Figures 10 and 12 to make a rough comparison of our results with the Hamana et al. (2004) simulations. If we cut both the SHELS cluster sample (open symbols in Figure 12) and the DLS detections (solid symbols in Figure 12) at $\nu > 4$ (upper dotted sensitivity curve), the completeness is $\sim 60\%$ and the efficiency (from Figure 10) is $\sim 43\%$. Here we include Peak 5 (the predicted lensing signal is well within the uncertainty of the $\nu = 4$ threshold) as a DLS/SHELS detection; we do not include x-ray cluster (solid star) in our evaluations of efficiency/completeness because detection requires a higher resolution map. Although there are only 7 weak lensing peaks with $\nu > 4$ and 5 clusters from SHELS which contribute to this assessment, we see the trend emphasized by Hamana et al. (2004); the fractional completeness of cluster identification exceeds the efficiency. If we make the comparison at $\nu = 3.5$ we have 12 weak lensing peaks and 8 SHELS clusters (again ignoring the x-ray cluster indicated by the solid star in Figure 12). The completeness is $\sim 50\%$ and the efficiency is $\sim 33\%$. Within the considerable uncertainties of the comparison, these results are consistent with the predictions of Hamana et al. (2004).

The DLS efficiency for cluster identification is consistent with the results of Schirmer et al. (2007) but inconsistent with the much greater efficiencies claimed by Miyazaki et al. (2007), Gavazzi & Soucail (2007) and Kubo et al. (2009). A major reason for a lower efficiency is rejection of systems with a velocity dispersion too low to account for the weak lensing signal; this rejection is obviously impossible without a dense redshift survey like SHELS. Another contributing factor in the comparison with Kubo et al. (2009) is the smaller offset we allow between the position of the lensing peak and the SHELS system.

We can push the comparison between the theory and our survey a bit further by considering detections as a function of redshift. In making this comparison, we take the greater mass threshold at greater redshift (see Figure 12) into account. Following the same approach, Hamana et al. (2004) find that there is no strong dependence of completeness on redshift (their Figure 20). In our survey, there is a one-to-one correspondence between the three lensing peaks and SHELS clusters at the peak sensitivity of both surveys ($z \sim 0.3$). At greater redshift the weak lensing survey is woefully incomplete although two of the five clusters which should be detected at $\nu > 3.5$ correspond to peaks in the weak lensing map with $\nu > 1.65$. The reasons for the non-detections at greater redshift are unclear, but may include the structure of the clusters, the details of the large-scale structure along the line-of-sight, and the properties of the noise in the DLS map. Small number statistics are also an obvious issue here, but the comparison between theory and observation certainly indicates issues worth further exploration.

7. Conclusion

We use a four square degree region of the DLS to compare the detection of massive clusters with a weak lensing convergence map and with a dense foreground redshift survey, SHELS. This comparison, based on a dense redshift survey completely covering the weak lensing field is the first of its kind.

We calculate the sensitivity of the DLS as a function of redshift to clusters of a particular rest frame line-of-sight velocity dispersion. We use this sensitivity curve to evaluate both the efficiency and completeness of the set of “projected mass selected” clusters corresponding to convergence peaks with signal-to-noise, $\nu \geq 3.5$. We conclude that the efficiency is 33% and the completeness is 50% for clusters more massive than $\sim 1.7 \times 10^{14} M_{\odot}$ (rest frame velocity dispersion $\gtrsim 600 \text{ km s}^{-1}$). These results agree with the more pessimistic previous evaluation of the efficacy of weak lensing by Schirmer et al. (2007) and they are consistent with ray tracing simulations by Hamana et al. (2004).

We examine the coincidence between DLS convergence map peaks with $\nu \gtrsim 1$ and clusters in SHELS with rest frame line-of-sight velocity dispersion $\gtrsim 500 \text{ km s}^{-1}$. For all nine coincidences, the offset between the position of the weak lensing peak and the cluster center in SHELS is less than $1.5'$. These small offsets are consistent with previous observations by Gavazzi & Soucail (2007), but smaller than the theoretical predictions of Dietrich et al. (2008). We use these offsets and the complete SHELS catalog to demonstrate that these coincidences are probably real detections even at low signal-to-noise; we note that two of these coincidences are SHELS clusters that should be detected in the DLS at greater significance. These latter coincidences indicate that failure to detect SHELS clusters in the DLS may be related to the properties of the noise in the κ map. We show that, as expected, the efficiency of the weak lensing survey for cluster detection decreases steeply with signal-to-noise.

X-ray observations cover only a small portion of the DLS field, thus limiting the evaluation of the efficiency and completeness of the DLS relative to an x-ray selected catalog. There are seven known extended cluster x-ray sources in the DLS field. Among these, three are DLS detections. The SHELS velocity dispersion indicates that the x-ray cluster XMMU J091935+303155 should be detected in the DLS, but it is not. SHELS provides velocity dispersions for the remaining three systems and suggests that none of them should produce a $\nu \geq 3.5$ peaks in the weak lensing map without significant boosting from large-scale structure superposed along the line-of-sight.

The SHELS/DLS weak lensing efficiency for cluster selection is more pessimistic than previous surveys at least in part because we require that the velocity dispersion measured in SHELS be adequate to produce the lensing signal. Previous evaluations of efficiency based

on counts and/or photometric redshifts by necessity include superpositions of systems with low velocity dispersion. We use SHELS to construct an example demonstrating the failure of photometric redshifts to distinguish between a massive cluster and a superposition of groups along the line-of-sight.

The underlying causes of the low efficiency and completeness of the weak lensing candidate list are hard to identify in our sample although the properties of the noise in the κ map are probably important. Although the clusters the DLS detects in SHELS are richer than the ones the DLS does not detect at redshifts of 0.4 — 0.55, this difference in optical properties is unlikely to account for the non-detections. There is also no obvious reason for the DLS failure to detect the x-ray cluster XMMU J091935+303155. Although the the conclusions of the DLS/SHELS comparison are obviously limited by small number statistics, they demonstrate that more extensive evaluation of both the efficiency and completeness of weak lensing cluster candidate lists relative to other catalogs is crucial for optimal application of weak lensing selected cluster catalogs to cosmology.

We thank P. Berlind and M. Calkins for their expert operation of the Hectospec. D. Mink, J. Roll, S. Tokarz, and W. Wyatt constructed and ran the Hectospec pipeline. We thank H. Khiabani and J. Kubo for guidance in using the DLS convergence maps. We thank the anonymous referee for insightful, careful, gracious comments that inspired us to improve the paper. We also thank S. Kenyon and M. Zaldarriaga for many insightful discussions. The Smithsonian Institution generously supported Hectospec and SHELS. Lucent Technologies and NSF grants AST 04-41-72 and AST 01-34753 generously supported the DLS. We appreciate generous allocations of telescope time on the Kitt Peak National Observatory 4 m telescope and on the MMT. I. Dell’Antonio is supported by NSF-AST grant AST-0708433.

Facilities: MMT(Hectospec), Mayall(MOSAIC-I and II widefield cameras)

REFERENCES

- Abell, G. O. 1958, *ApJS*, 3, 211
- Abell, G. O., Corwin, H. G., Jr., & Olowin, R. P. 1989, *ApJS*, 70, 1
- Bergé, J., et al. 2008, *MNRAS*, 385, 695
- Böhringer, H., et al. 2004, *A&A*, 425, 367
- Dietrich, J. P., Erben, T., Lamer, G., Schneider, P., Schwobe, A., Hartlap, J., & Maturi, M. 2007, *A&A*, 470, 821
- Casertano, S., et al. 2000, *AJ*, 120, 2747
- Ebeling, H., Voges, W., Böhringer, H., Edge, A. C., Huchra, J. P., & Briel, U. G. 1996, *MNRAS*, 281, 799
- Edge, A. C., Stewart, G. C., Fabian, A. C., & Arnaud, K. A. 1990, *MNRAS*, 245, 559
- Fabricant, D. G., Hertz, E. N., Szentgyorgyi, A. H., Fata, R. G., Roll, J. B., & Zajac, J. M. 1998, *Proc. SPIE*, 3355, 285
- Fabricant, D., et al. 2005, *PASP*, 117, 1411
- Gavazzi, R., & Soucail, G. 2007, *A&A*, 462, 459
- Geller, M. J., Dell’Antonio, I. P., Kurtz, M. J., Ramella, M., Fabricant, D. G., Caldwell, N., Tyson, J. A., & Wittman, D. 2005, *ApJ*, 635, L125
- Hamana, T., Takada, M., & Yoshida, N. 2004, *MNRAS*, 350, 893
- Hamana, T., Miyazaki, S., Kashikawa, N., Ellis, R. S., Massey, R. J., Refregier, A., & Taylor, J. E. 2009, *PASJ*, 61, 833
- Hennawi, J. F., & Spergel, D. N. 2005, *ApJ*, 624, 59
- Hetterscheidt, M., Erben, T., Schneider, P., Maoli, R., van Waerbeke, L., & Mellier, Y. 2005, *A&A*, 442, 43
- Khiabani, H., & Dell’Antonio, I. P. 2008, *ApJ*, 684, 794
- Koester, B. P., et al. 2007, *ApJ*, 660, 239
- Kubo, J. M., Khiabani, H., Dell’Antonio, I. P., Wittman, D., & Tyson, J. A. 2009, *ApJ*, 702, 980

- Kurtz, M. J., Geller, M. J., Fabricant, D. G., Wyatt, W. F., & Dell’Antonio, I. P. 2007, *AJ*, 134, 1360
- Kurtz, Michael J. et al. 2010, in prep.
- Kurtz, M. J., & Mink, D. J. 1998, *PASP*, 110, 934
- Leauthaud, A., et al. 2007, *ApJS*, 172, 219
- Lin, Y.-T., Mohr, J. J., & Stanford, S. A. 2004, *ApJ*, 610, 745
- Maturi, M., Schirmer, M., Meneghetti, M., Bartelmann, M., & Moscardini, L. 2007, *A&A*, 462, 473
- Maturi, M., Angrick, C., Bartelmann, M., & Pace, F. 2009, arXiv:0907.1849
- Mellier, Y. 1999, *ARA&A*, 37, 127
- Mink, D. J., Wyatt, W. F., Caldwell, N., Conroy, M. A., Furesz, G., & Tokarz, S. P. 2007, *Astronomical Data Analysis Software and Systems XVI*, 376, 249
- Miyazaki, S., et al. 2002, *ApJ*, 580, L97
- Miyazaki, S., Hamana, T., Ellis, R. S., Kashikawa, N., Massey, R. J., Taylor, J., & Refregier, A. 2007, *ApJ*, 669, 714
- Mobasher, B., et al. 2007, *ApJS*, 172, 117
- Muller, G. P., Reed, R., Armandroff, T., Boroson, T. A., & Jacoby, G. H. 1998, *Proc. SPIE*, 3355, 577
- Padmanabhan, N., et al. 2005, *MNRAS*, 359, 237
- Piccinotti, G., Mushotzky, R. F., Boldt, E. A., Holt, S. S., Marshall, F. E., Serlemitsos, P. J., & Shafer, R. A. 1982, *ApJ*, 253, 485
- Press, W. H., Teukolsky, S. A., Vetterling, W. T., & Flannery, B. P. 1992, Cambridge: University Press, —c1992, 2nd ed.,
- Ramella, M. et al. 2010, in prep.
- Rines, K., & Diaferio, A. 2006, *AJ*, 132, 1275
- Rines, K., Geller, M. J., Kurtz, M. J., & Diaferio, A. 2003, *AJ*, 126, 2152

- Roll, J. B., Fabricant, D. G., & McLeod, B. A. 1998, *Proc. SPIE*, 3355, 324
- Schirmer, M., Erben, T., Hettterscheidt, M., & Schneider, P. 2007, *A&A*, 462, 875
- Schneider, P. 2006, *Gravitational Lensing: Strong, Weak and Micro*, Saas-Fee Advanced Courses, Volume 33. ISBN 978-3-540-30309-1. Springer-Verlag Berlin Heidelberg, 2006, p. 269, 269
- Schwartz, D. A. 1978, *ApJ*, 220, 8
- Sehgal, N., Hughes, J. P., Wittman, D., Margoniner, V., Tyson, J. A., Gee, P., & dell’Antonio, I. 2008, *ApJ*, 673, 163
- Spergel, D. N., et al. 2007, *ApJS*, 170, 377
- Taniguchi, Y., et al. 2007, *ApJS*, 172, 9
- Williams, R. E., et al. 1996, *AJ*, 112, 1335
- Wittman, D. M., et al. 2002, *Proc. SPIE*, 4836, 73
- Wittman, D., Tyson, J. A., Margoniner, V. E., Cohen, J. G., & Dell’Antonio, I. P. 2001, *ApJ*, 557, L89
- Wittman, D., Dell’Antonio, I. P., Hughes, J. P., Margoniner, V. E., Tyson, J. A., Cohen, J. G., & Norman, D. 2006, *ApJ*, 643, 128
- Zwicky, F., Herzog, E., & Wild, P. 1968, ‘Catalogue of Galaxies and of Clusters of Galaxies,’ Pasadena: California Institute of Technology (CIT), 1961-1968

Table 1. Velocity Dispersions of SHELS/DLS Candidate Clusters

SHELS Name	DLS Rank	ν_{DLS}	RA ₂₀₀₀	DEC ₂₀₀₀	z	$\sigma_{los,3}$ km/s	N ₃	err ₃ km/s	$\sigma_{los,6}$ km/s	N ₆	err ₆ km/s
SHELS J0915.1+2954	-	-	9:15:03.5	29:54:09	0.1319	565	11	134	505	16	130
SHELS J0916.0+3028	10	3.76	9:15:57.1	29:49:42	0.1844	500	17	99	565	38	71
SHELS J0916.2+2949 ^D	10	3.76	9:16:10.9	29:48:44	0.5343	880	11	127	867	29	71
SHELS J0916.3+2916	17	2.69	9:16:19.2	29:15:47	0.5347	587	8	74	642	14	70
SHELS J0916.7+2920	34	1.97	9:16:40.1	29:19:52	0.2158	595	16	75	569	26	75
SHELS J0916.8+2908	-	-	9:16:50.0	29:08:19	0.3356	591	7	61	532	10	61
SHELS J0916.9+3003	-	-	9:16:56.7	30:03:08	0.3189	487	18	68	442	42	49
SHELS J0918.1+3038 ^D	42	1.65	9:18:05.8	30:37:48	0.3970	686	10	147	749	21	101
SHELS J0918.2+3057 ^D	-	-	9:18:09.8	30:56:56	0.4244	667	9	125	732	16	124
SHELS J0918.3+3024	-	-	9:18:16.0	30:24:07	0.1241	539	25	74	534	53	53
SHELS J0918.6+2953 ^D	5	4.48	9:18:38.6	29:53:22	0.3178	729	41	90	676	66	63
SHELS J0919.6+3032 ^{*D}	-	-	9:19:33.3	30:31:59	0.4273	596	11	107	718	19	113
SHELS J0920.1+3010	-	-	9:20:03.6	30:10:06	0.4263	507	8	81	541	12	68
SHELS J0920.4+3030 ^{*D}	2	5.72	9:20:22.5	30:30:29	0.3004	-	-	-	929	219	200
SHELS J0920.9+3029 ^{*D}	1	6.64	9:20:55.6	30:28:38	0.2915	-	-	-	856	132	200
SHELS J0921.0+2942	-	-	9:20:59.6	29:42:00	0.2964	463	28	75	551	49	50
SHELS J0921.2+3028 [*]	-	-	9:21:12.7	30:28:08	0.4265	754	22	92	772	40	88
SHELS J0921.3+2946	-	-	9:21:13.9	29:45:37	0.3834	662	11	150	549	18	131
SHELS J0921.4+2958 ^D	15	2.87	9:21:24.9	29:58:12	0.4318	597	15	94	818	24	109
SHELS J0923.6+2929	33	1.97	9:23:38.0	29:28:35	0.2216	493	23	68	454	40	46

^{*}These clusters are the known extended x-ray sources XMMU J091935+303155, CXOU J092026+302938, CXOU J092053+302800, and CXOU J092110+302751. They also appear in Table 2

^DThe SHELS velocity dispersion implies that these clusters should be detected at $\nu_{DLS} \geq 3.5$ with the resolution of the DLS map we use. See Figure 12

Table 2. Properties of Known SHELS/DLS X-Ray Clusters

X-ray Name	DLS Rank	RA ₂₀₀₀	DEC ₂₀₀₀	z	$\sigma_{los,3}$ km/s	N ₃	err ₃ km/s	Xray Flux ^a 10 ⁻¹⁴ erg s ⁻¹ cm ⁻²
CXOU J091551+293637	11	9:15:51.8	29:36:37	0.5312	361	11	70	1.80
—	11 ^b	9:15:51.8	29:36:37	0.1851	420	8	144	1.80
CXOU J091554+293316	8 ^b	9:15:54.4	29:33:16	0.1847	526	8	105	0.71
CXOU J091601+292750	-	9:16:01.1	29:27:50	0.5319	523	7	126	1.80
—	- ^b	9:16:01.1	29:27:50	0.1834	593	5	71	1.80
XMMU J091935+303155	-	9:19:35.0	30:31:55	0.4273	596	11	107	-
CXOU J092026+302938	2	9:20:26.4	30:29:39	0.3004	929 ^c	219 ^c	200 ^c	64.20
CXOU J092053+302800	1	9:20:53.0	30:28:00	0.2915	856 ^c	132 ^c	200 ^c	11.60
CXOU J092110+302751	-	9:21:10.3	30:27:52	0.4265	754	222	92	9.47

^a*Chandra* 0.5-2 keV flux from Table 3 of Wittman et al. (2006)

^bFor these entries we list the number of galaxies within the intercepted large-scale structure. The velocity dispersion refers to the effective velocity width of these structures rather than to a centrally concentrated group or cluster.

^cThe line-of-sight velocity dispersions and errors derived from the 6' samples as in Table 1

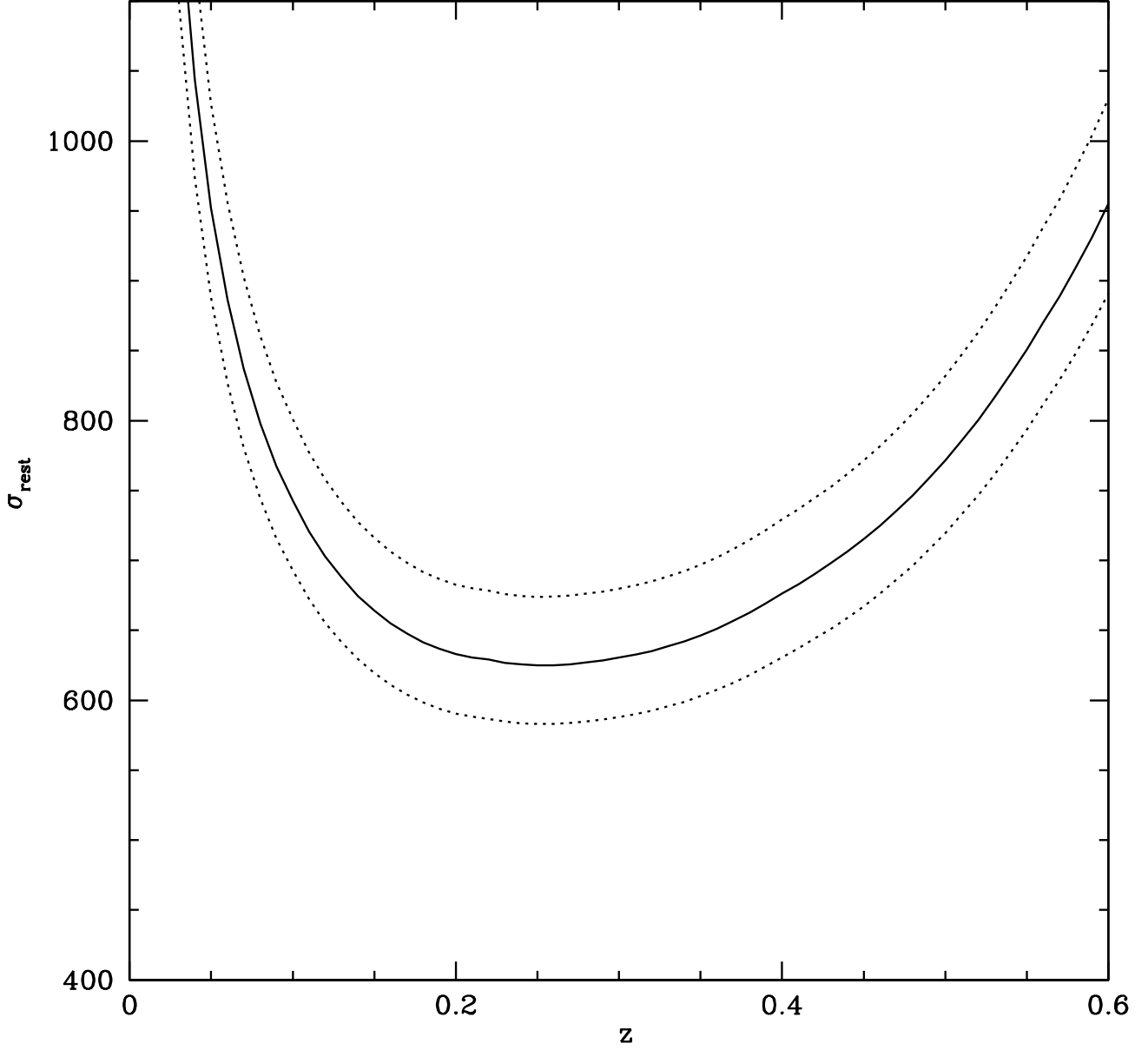


Fig. 1.— DLS sensitivity as a function of redshift. The solid curve shows the $\nu = 3.5$ detection limit. The dashed curves $\nu = 3$ (lower curve) and $\nu = 4$ (upper curve).

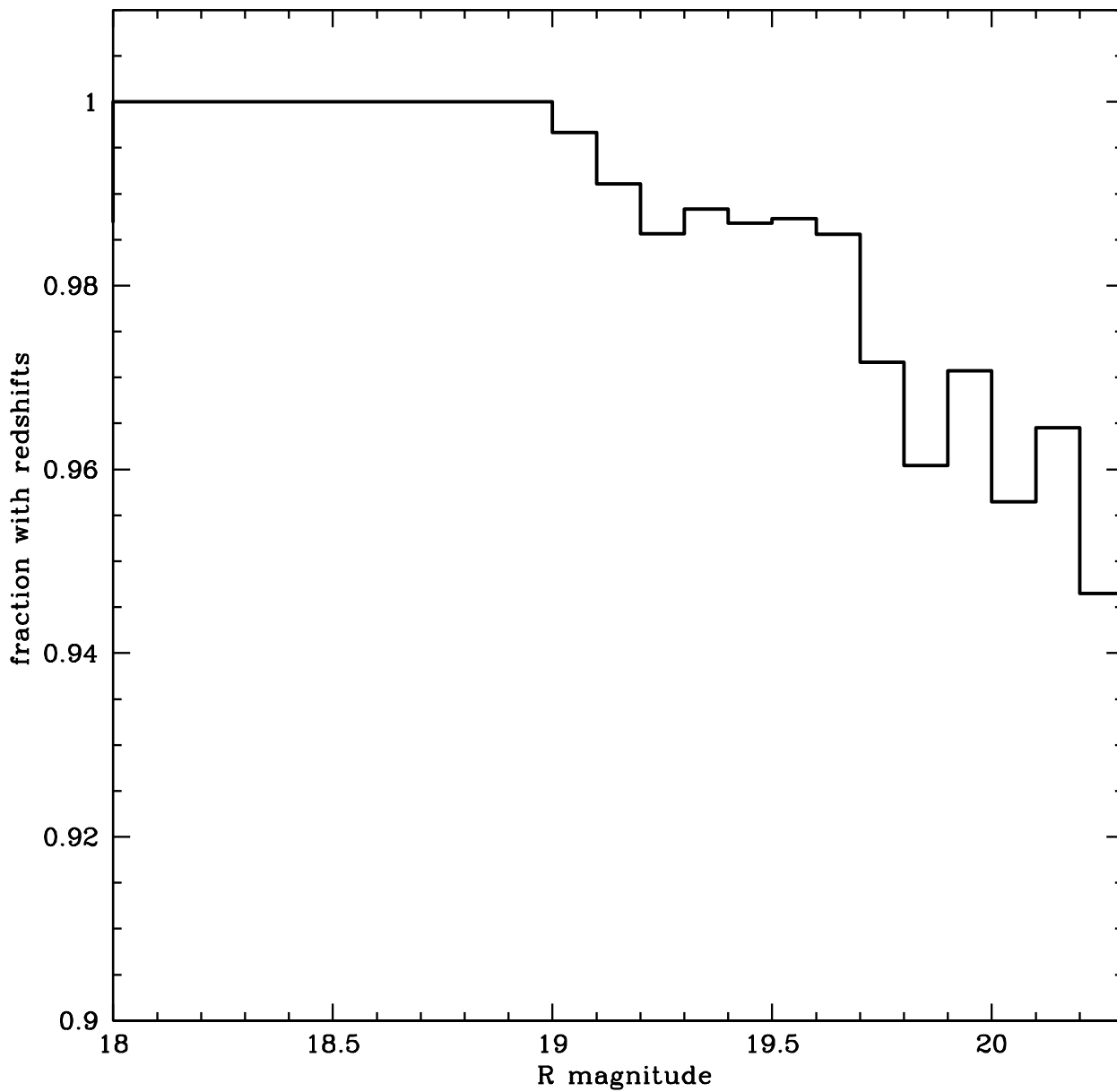


Fig. 2.— Completeness of the SHELS redshift survey. The redshift survey contains 9825 galaxies with $R \leq 20.3$. The integral completeness to $R = 20.3$ is 97.8%.

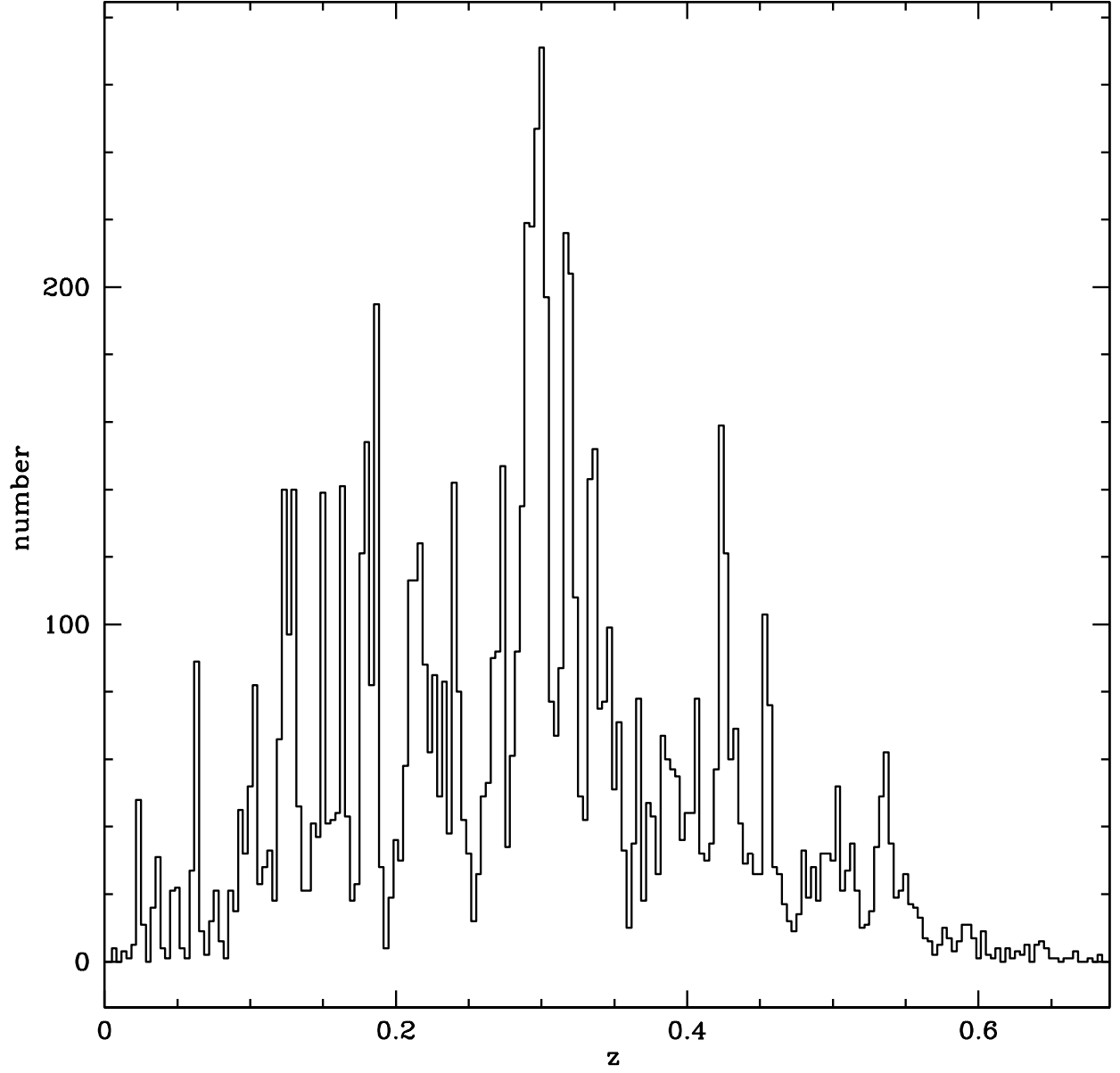


Fig. 3.— Redshift distribution for the SHELS redshift survey. The peaks are the standard signature of large-scale structure.

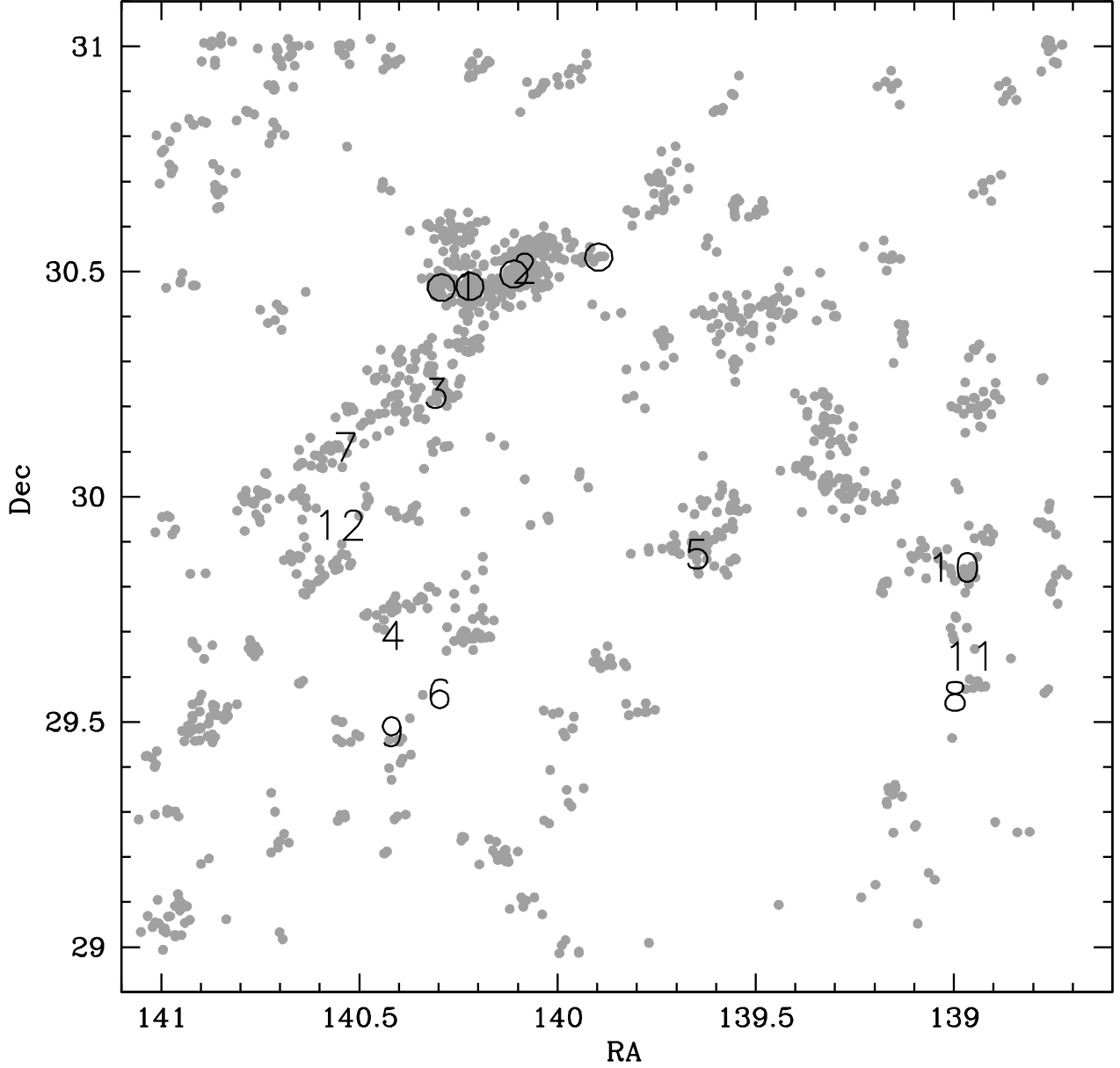


Fig. 4.— Map of F2 centers of the $3'$ radius $5\sigma_{SH}$ probes (gray dots) showing, x-ray clusters at $z = 0.28 - 0.43$ (open circles), and centers of significant weak lensing peaks (numbers). The value of the number gives the rank of the convergence map peak. Note the general correspondence between weak lensing peaks and $5\sigma_{SH}$ probes. Note that the tick marks on the declination axis are $6'$ apart, the diameter of the probes.

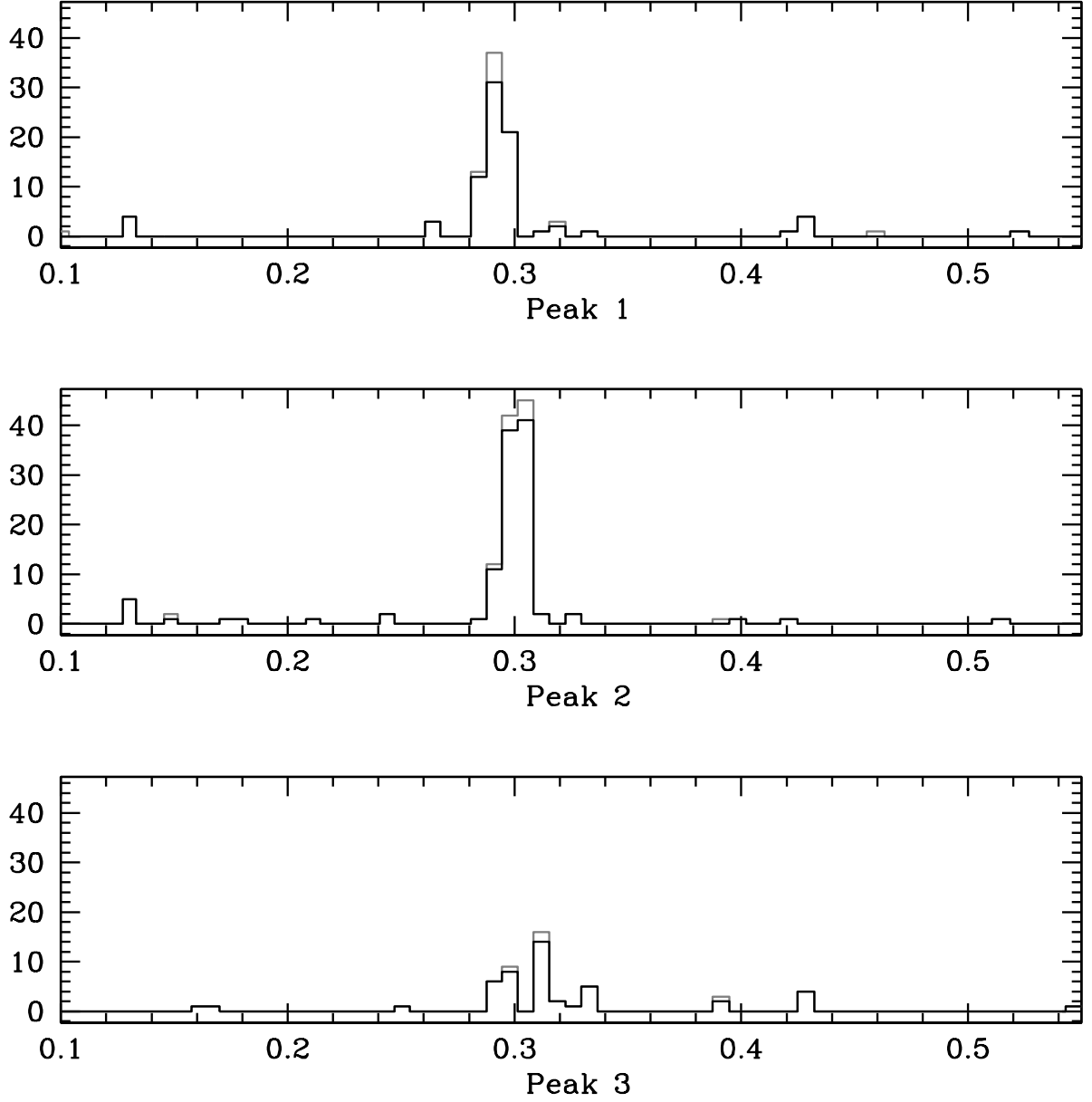


Fig. 5.— Redshift histograms of galaxies within $3'$ radius cones centered on DLS weak lensing peaks ranked 1 – 3. Bins in redshift are $0.0053(1+z)$. Black histograms include galaxies with $R \leq 20.3$; gray histograms include galaxies with $R \leq 20.6$.

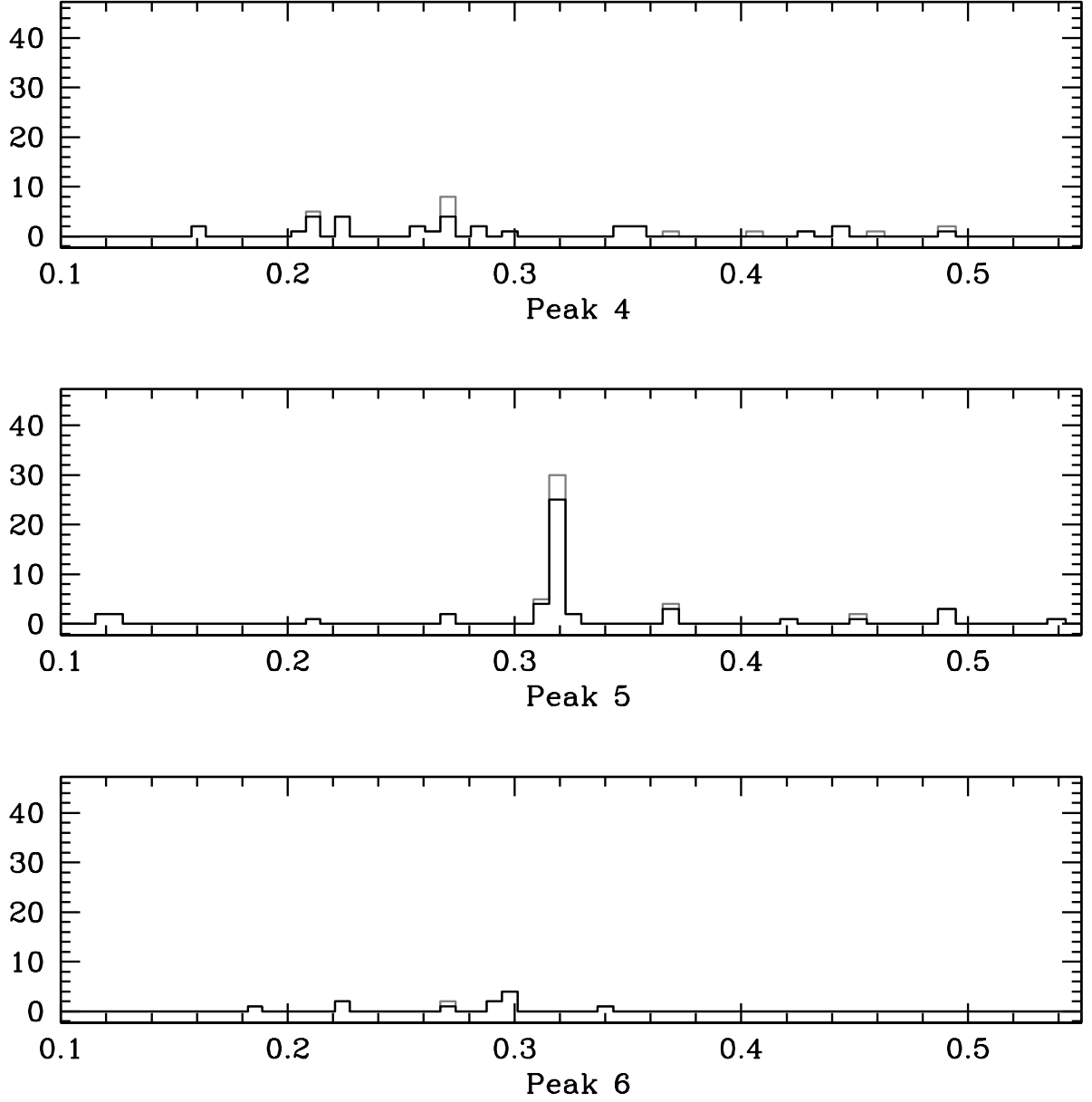


Fig. 6.— Redshift histograms of galaxies within $3'$ radius cones centered on DLS weak lensing peaks ranked 4 – 6. Bins in redshift are $0.0053(1+z)$. Black histograms include galaxies with $R \leq 20.3$; gray histograms include galaxies with $R \leq 20.6$.

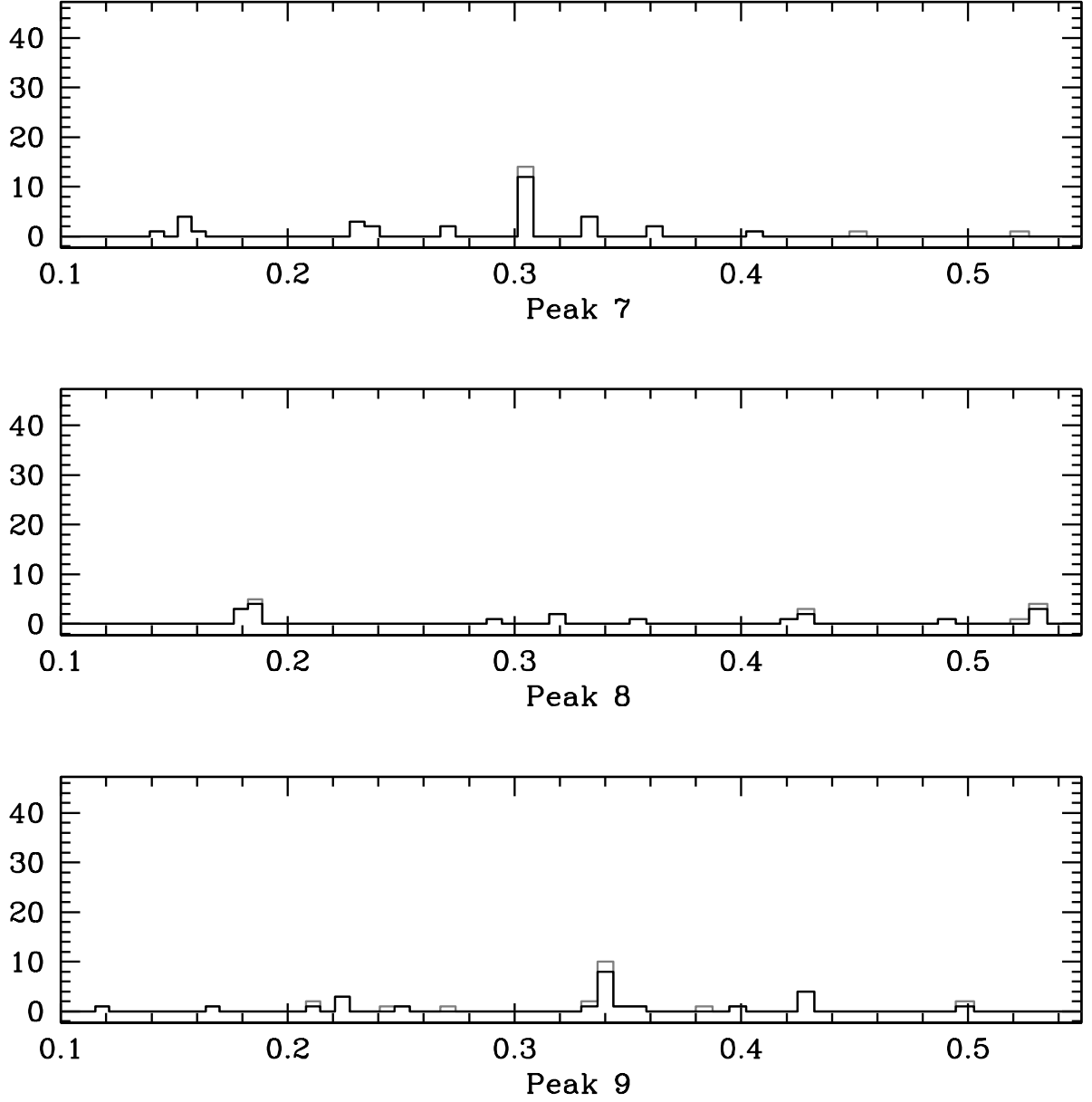


Fig. 7.— Redshift histograms of galaxies within $3'$ radius cones centered on DLS weak lensing peaks ranked 7 – 9. Bins in redshift are $0.0053(1+z)$. Black histograms include galaxies with $R \leq 20.3$; gray histograms include galaxies with $R \leq 20.6$.

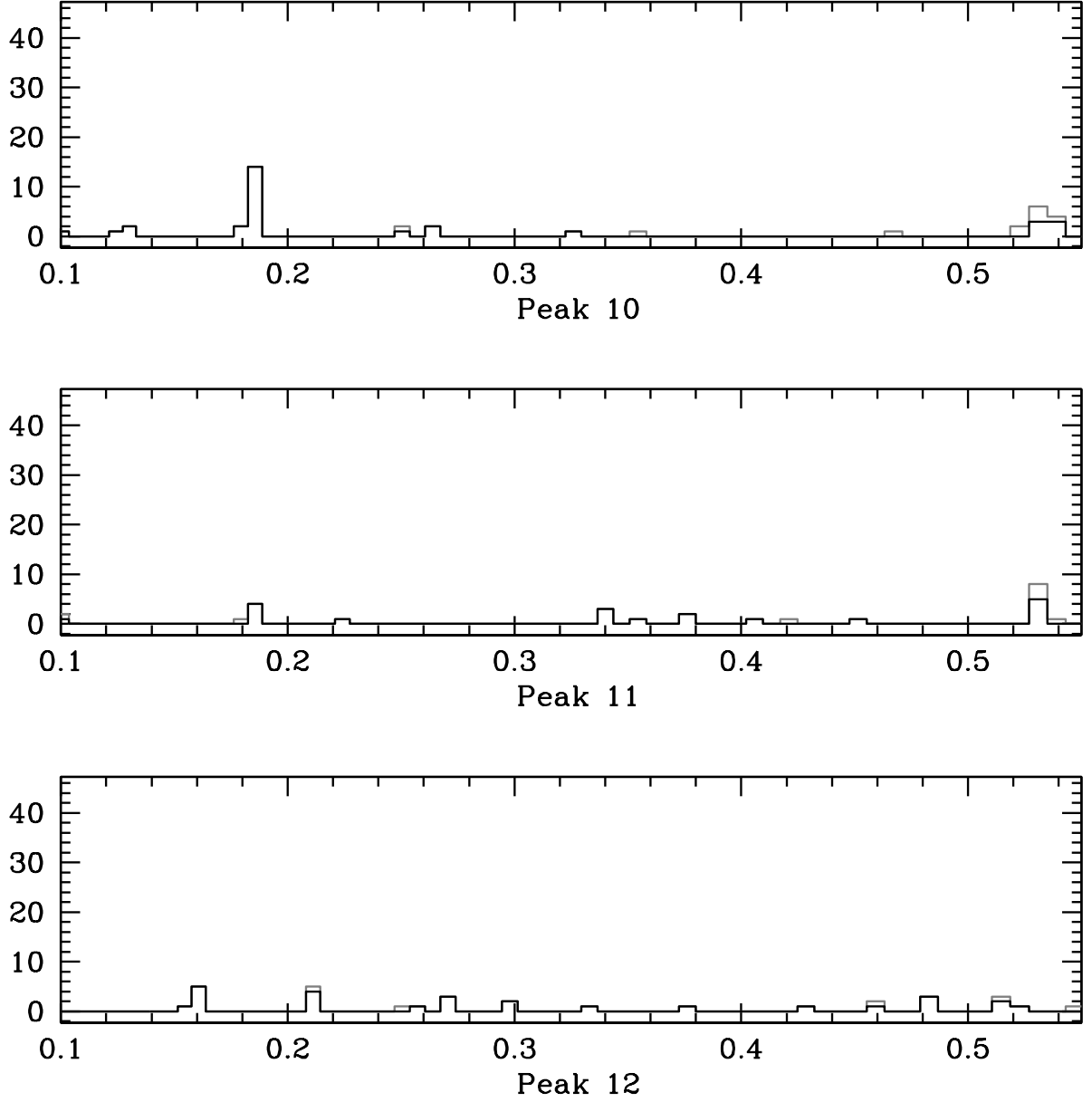


Fig. 8.— Redshift histograms of galaxies within 3' radius cones centered on DLS weak lensing peaks ranked 10 – 12. Bins in redshift are $0.0053(1+z)$. Black histograms include galaxies with $R \leq 20.3$; gray histograms include galaxies with $R \leq 20.6$.

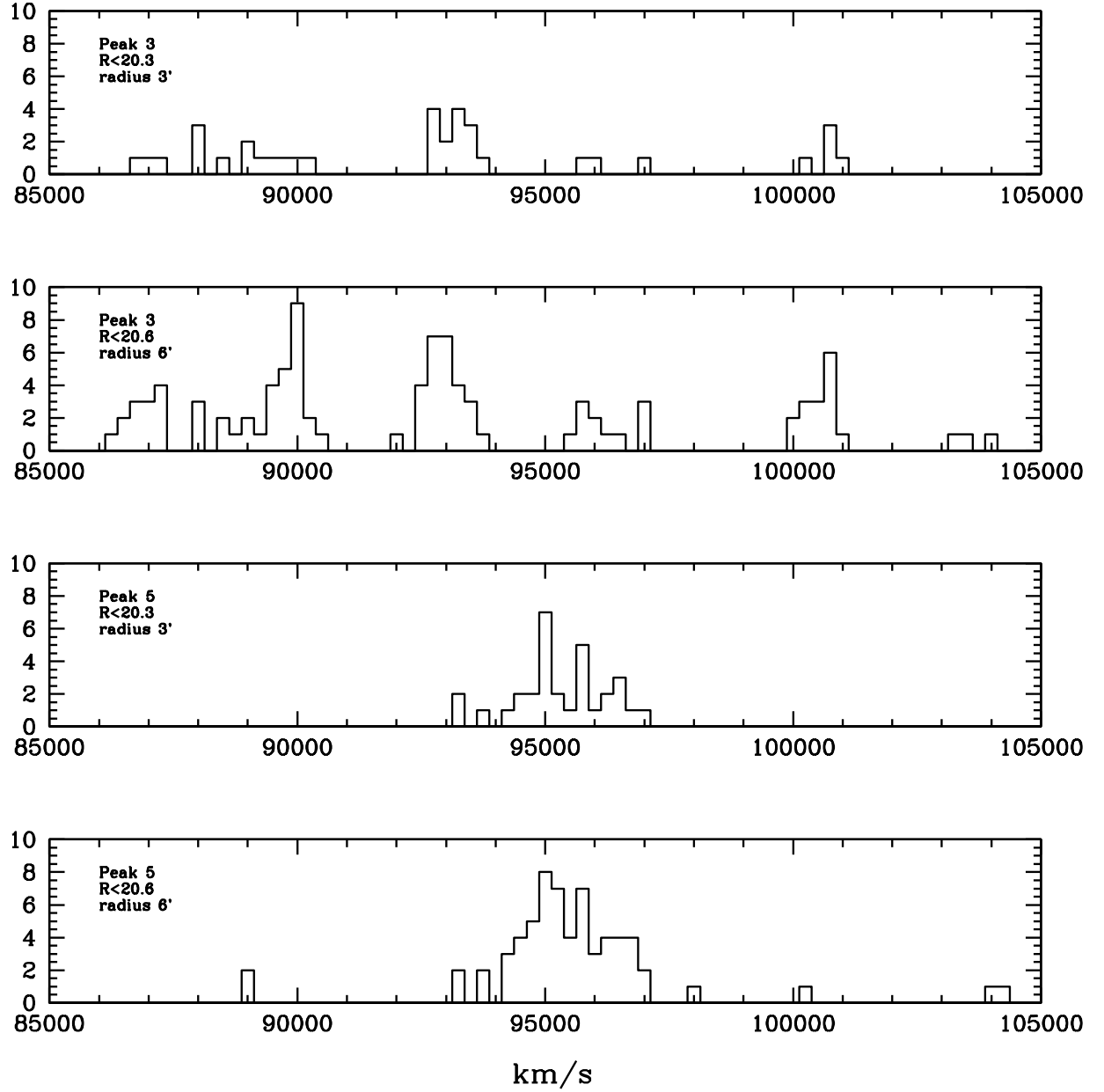


Fig. 9.— Comparison of the redshift distributions of galaxies toward DLS convergence peaks ranked 3 and 5. The upper panels show the line-of-sight redshift distribution within a 3' radius cone toward peak 3 for $R < 20.3$ and within a 6' radius cone to the deeper limit $R < 20.6$. The lower two panels show the analogous 3' and 6' line-of-sight redshift distributions for peak 5. Peak 5 is a rich cluster; peak 3 is a superposition.

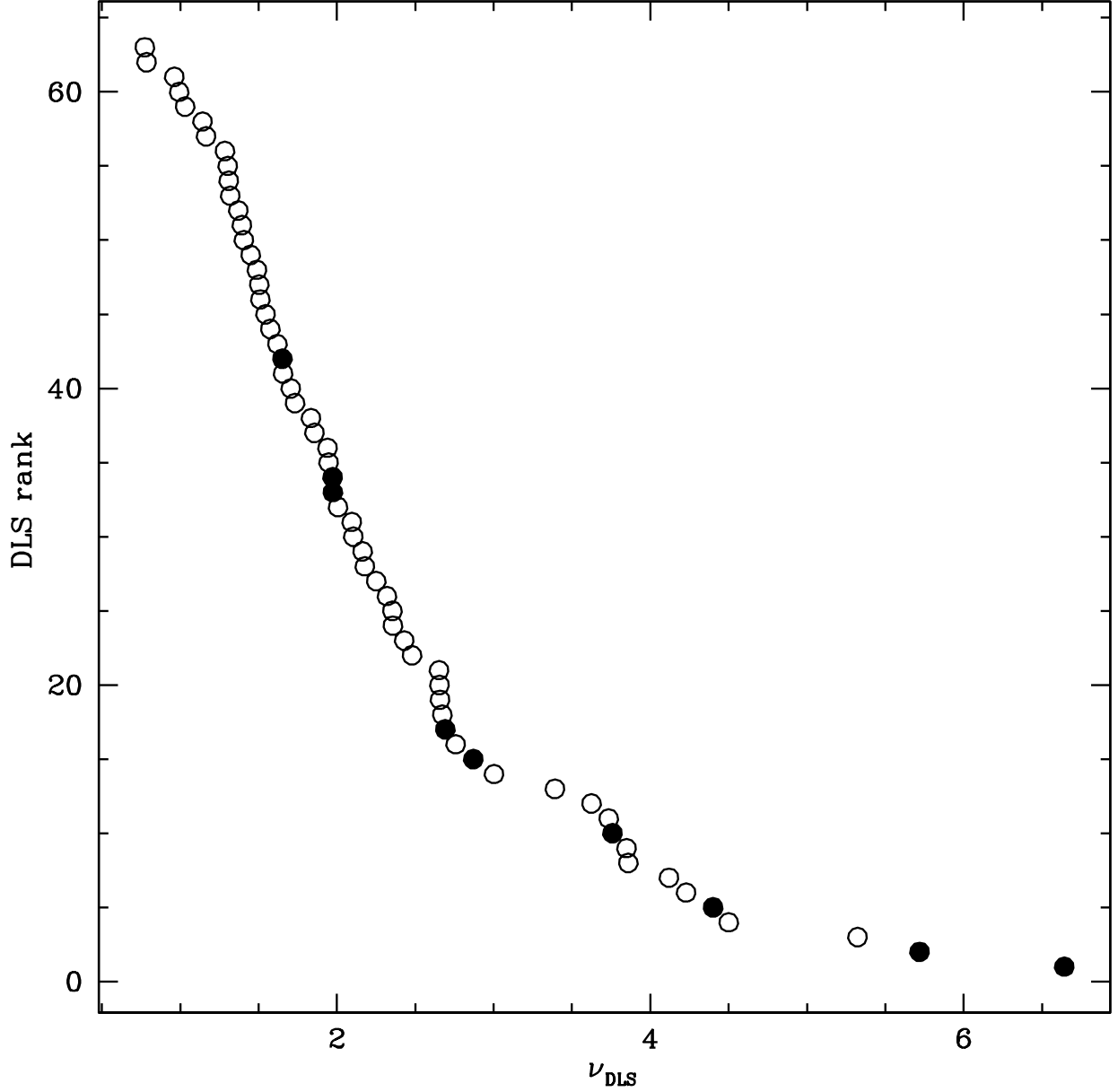


Fig. 10.— Rank as a function of ν for weak lensing peaks in the F2 field. Filled circles indicate coincidence of a SHELS cluster with $\sigma_{\text{los}} \gtrsim 500 \text{ km s}^{-1}$. There are no SHELS clusters with $\sigma_{\text{los}} \gtrsim 500 \text{ km s}^{-1}$ along the line-of-sight toward peaks designated with empty circles. Among the 12 DLS peaks with $\nu \geq 3.5$, only 4 correspond to massive SHELS clusters, an efficiency of 33%.

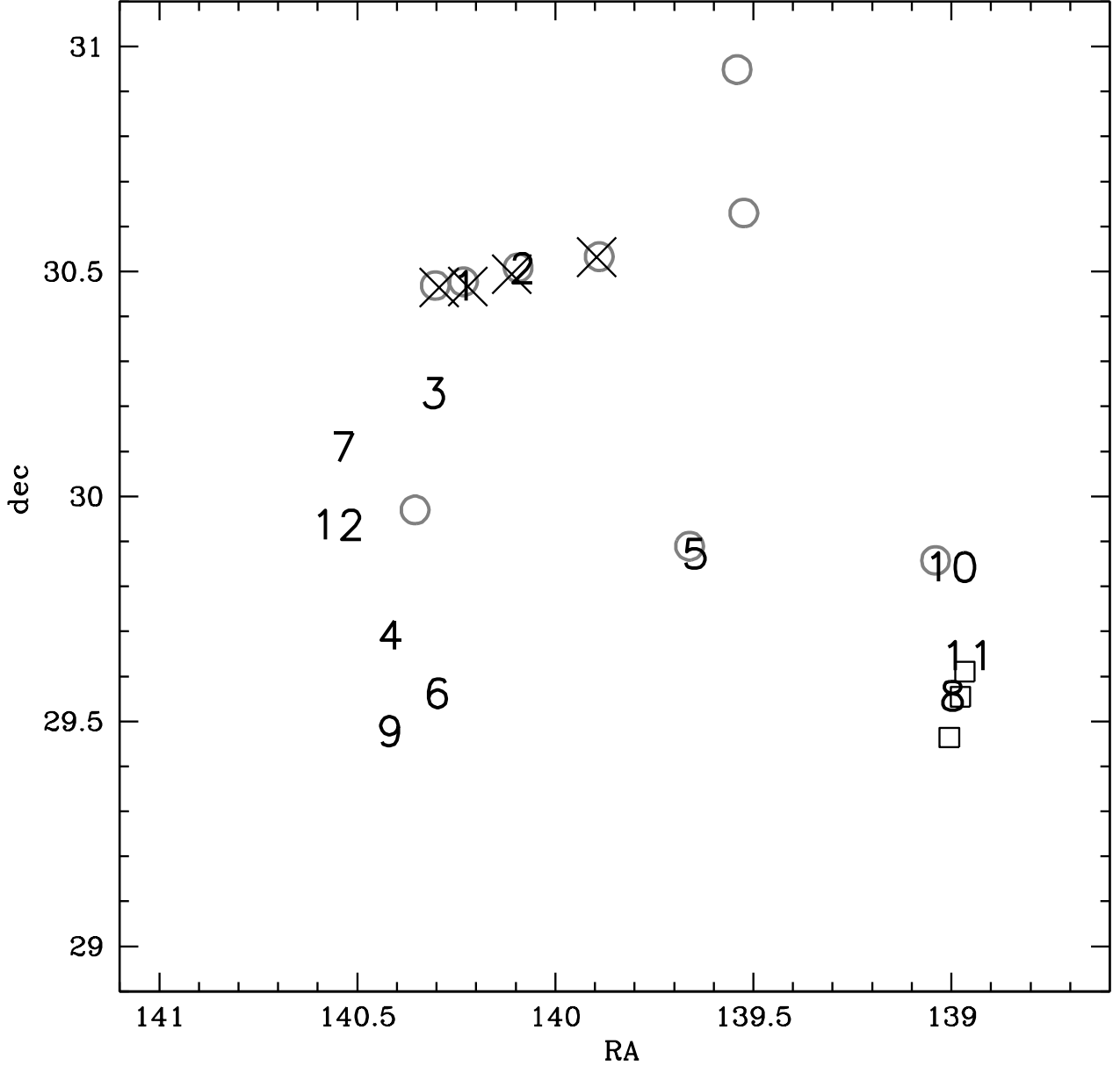


Fig. 11.— Map of the DLS field showing the positions of known x-ray clusters (crosses and open boxes), significant weak lensing peaks (numbers), and candidate SHELS clusters that lie above the threshold for detection in the weak lensing map (open circles; see Figure 12). Crosses denote the clusters CXOU J092026+302938, CXOU J092053+302900, CXOU J092026+302938, CXOU J092053+302900, and XMMU J091935+303155; all of these clusters are detected in SHELS and should be detected by weak lensing. Open boxes denote the x-ray sources CXOU J091551+293637, CXOU J091554+293316, and CXOU J091601+292750. There is no convincing optical counterpart to the central cluster of these three; the other two have SHELS velocity dispersions too low to place them above the lensing detection threshold in Figure 12. Open circles designate SHELS clusters (D in Table 1) that lie above the DLS detection threshold.

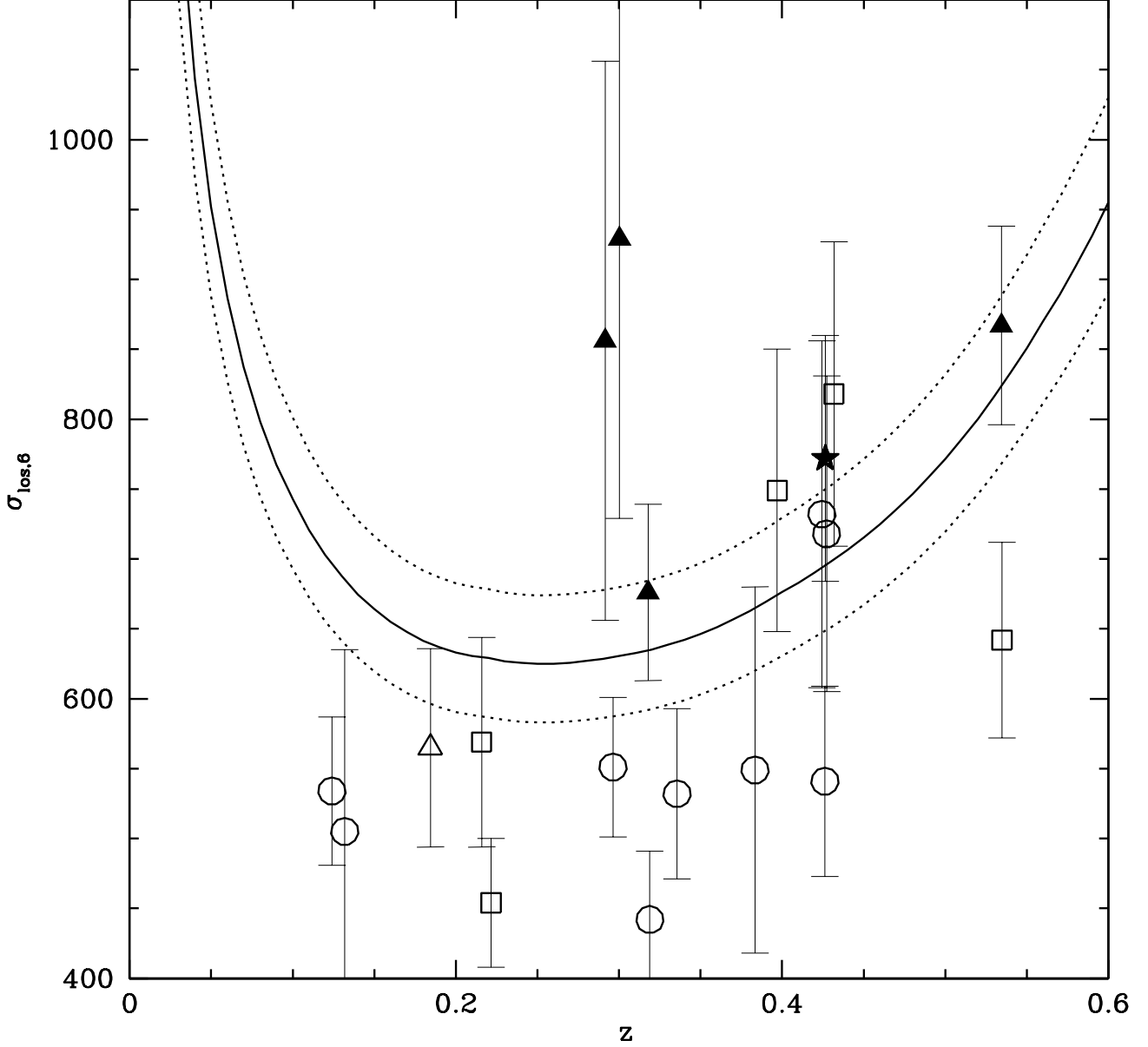


Fig. 12.— SHELS clusters and DLS sensitivity. The solid curve shows the $\nu = 3.5$ sensitivity as a function of redshift and the dotted lines indicate the $\nu = 3$ to $\nu = 4$ range from Figure 1. The vertical axis is rest frame line-of-sight velocity dispersion, $\sigma_{los,6}$. Filled triangles are DLS clusters coincident with $\nu \geq 3.5$ weak lensing peaks. Open squares are DLS systems coincident with lower DLS peaks in the range $1 \leq \nu < 3.5$. Open circles are SHELS clusters with no DLS counterpart. The filled star indicates the x-ray cluster XMMU J091935+303155 detected only in a higher resolution DLS map at $\nu = 5.7$. Among the massive clusters that lie above the $\nu = 3.5$ threshold, the DLS detects $\sim 50\%$.

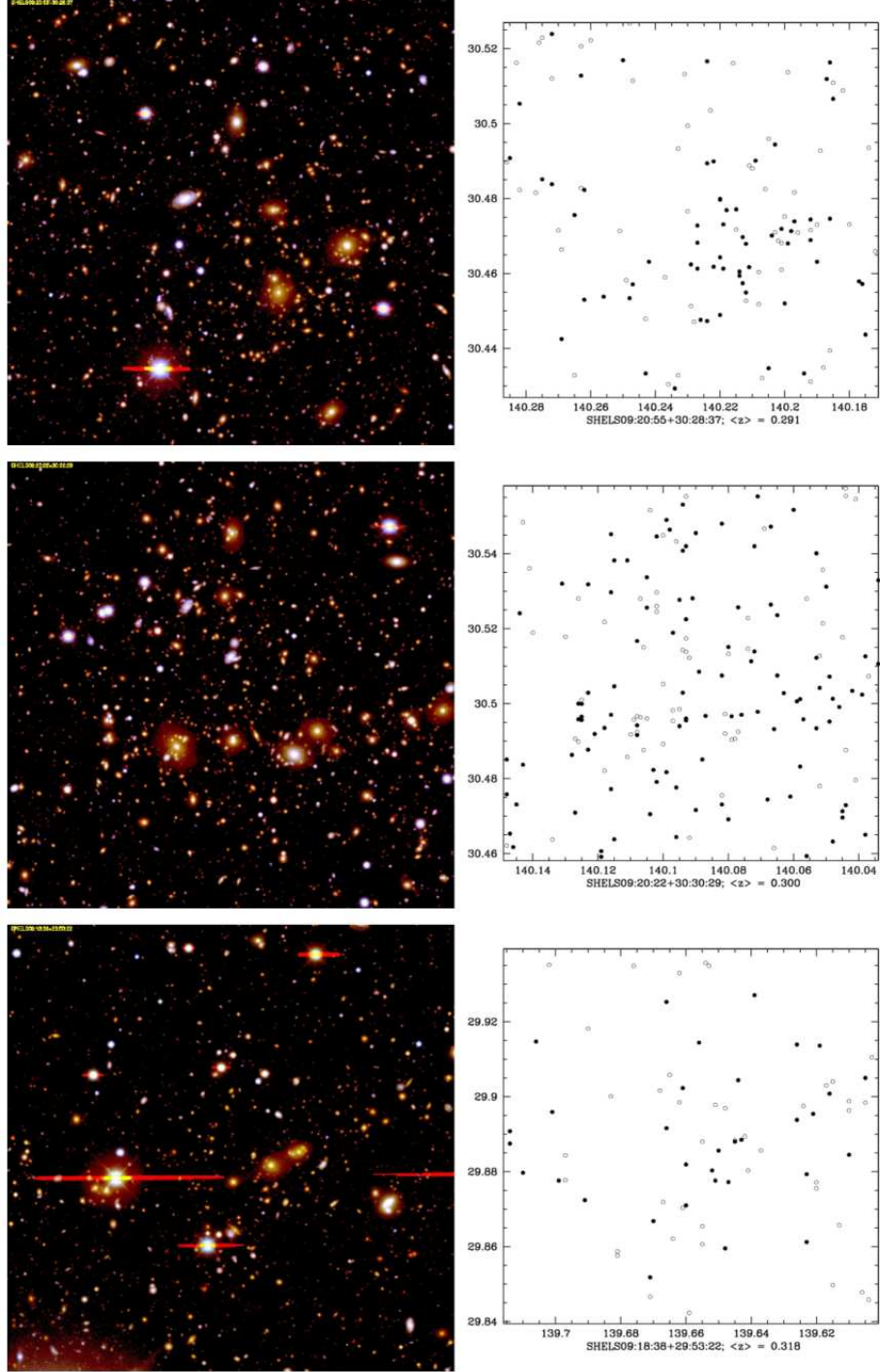


Fig. 13.— DLS images of the central $6' \times 6'$ regions of SHELS cluster candidates that should be detected at $\nu \geq 3.5$. SHELS J0920.9+3029 (top) is DLS peak 1; SHELS J0920.4+3030 (middle) is DLS peak 2; SHELS J0918.6+2953 (bottom) is DLS peak 5. The plots on the right correspond to the images on the left and show galaxies with redshifts in SHELS; the solid dots are system members. The redshift range for these three systems is 0.291 (top) to 0.318 (bottom).

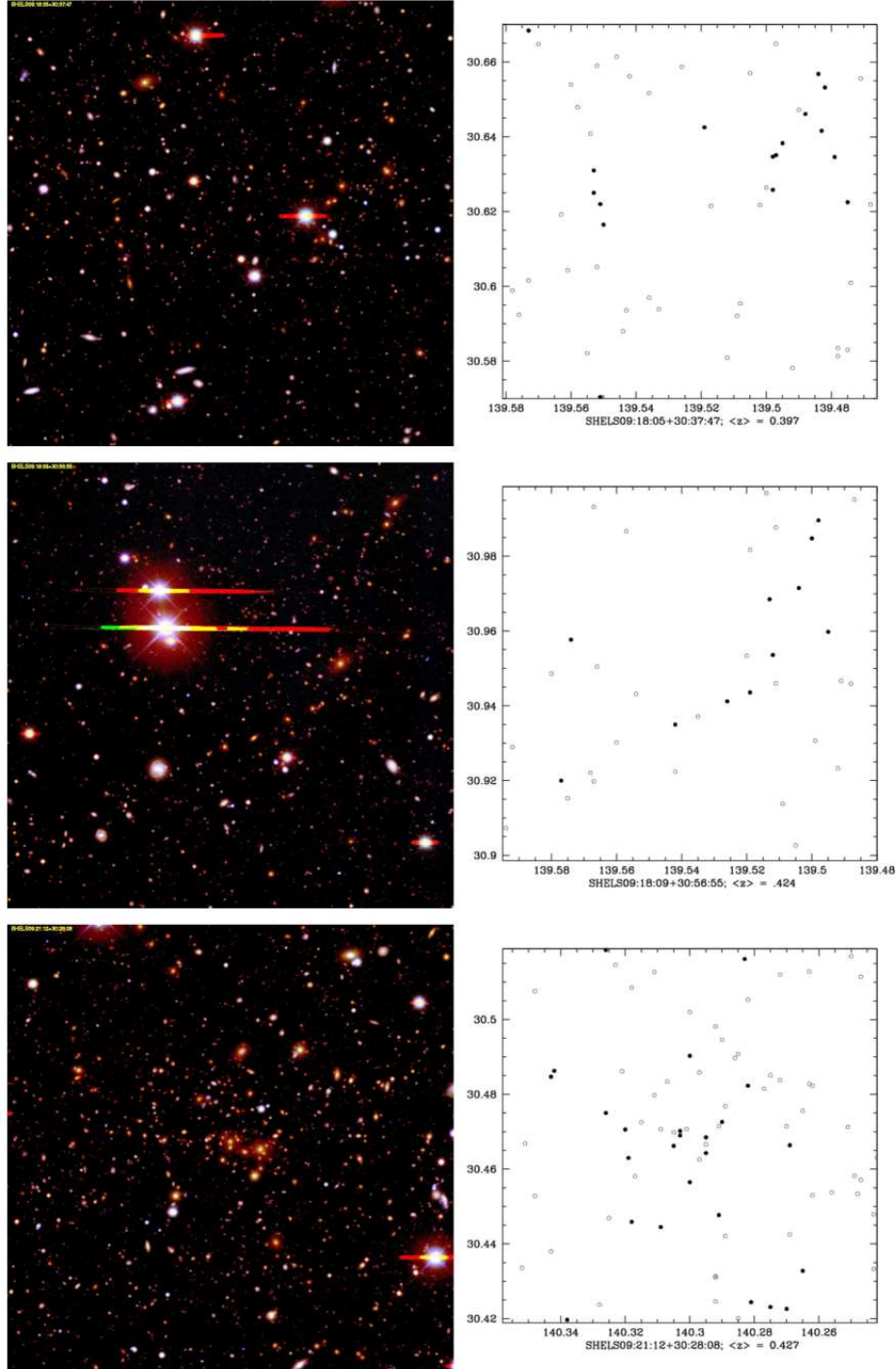


Fig. 14.— DLS images of the central $6' \times 6'$ regions of SHELS cluster candidates that should be detected at $\nu \geq 3.5$. SHELS J0918.1+3038 (top) is DLS peak 42; SHELS J0918.2+3057 (center) is undetected; SHELS J0921.2+3028 (bottom) is an extended x-ray source (CXOU J092110+302751) detected by the DLS in a higher resolution map. The plots on the right correspond to the images on the left and show galaxies with redshifts in SHELS; the solid dots are system members. The redshift range for these systems is 0.397 (top) to 0.427 (bottom).

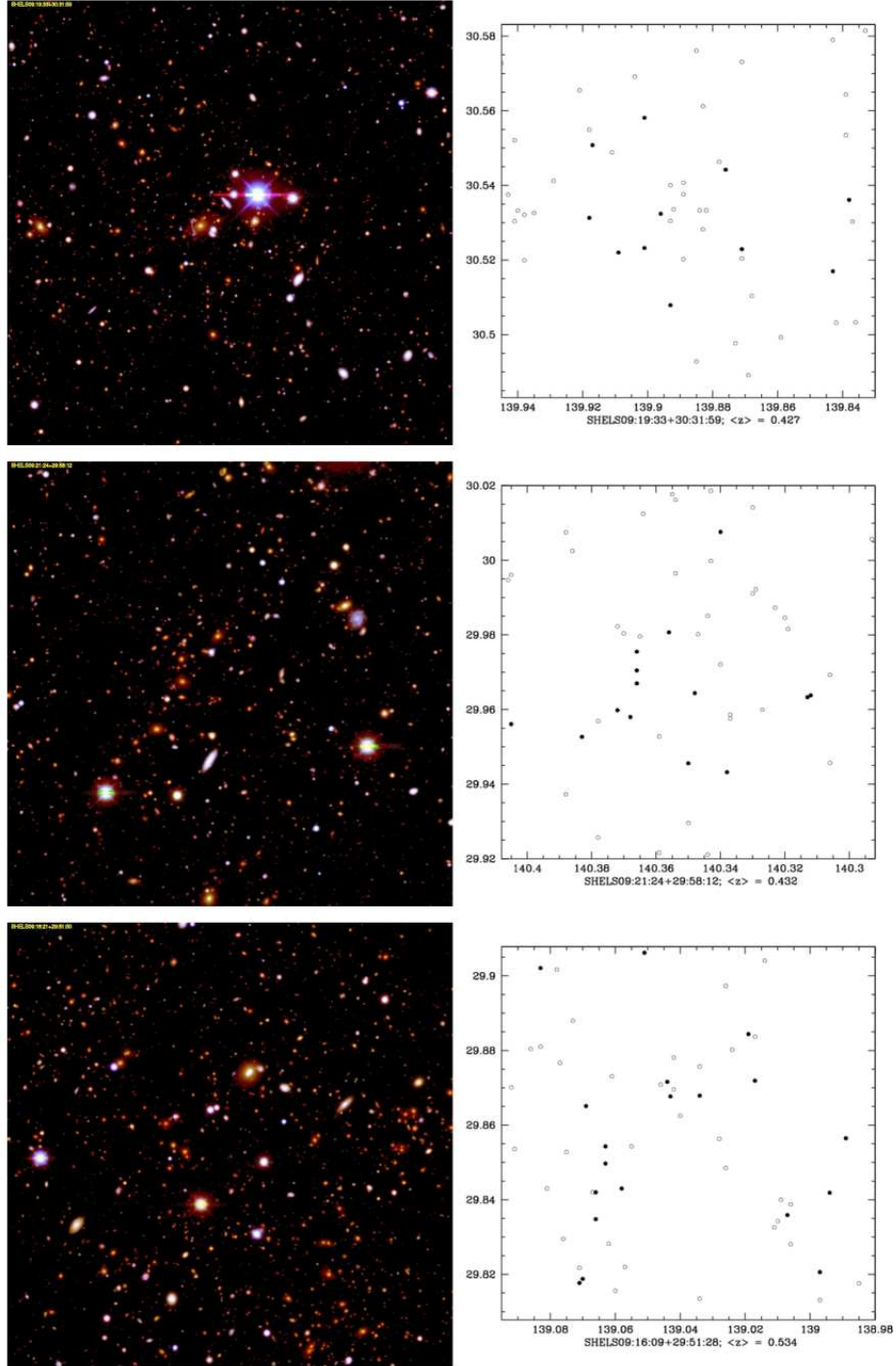


Fig. 15.— DLS images of the central $6' \times 6'$ regions of SHELS cluster candidates that should be detected at $\nu \geq 3.5$. SHELS J0919.6+3032 (top) is an extended x-ray source (XMMU J091935+303155) but is undetected by the DLS; SHELS J0921.4+2958 (middle) is DLS peak 15; SHELS J0916.2+2949 (bottom) is DLS peak 10. The plots on the right correspond to the images on the left and show galaxies with redshifts in SHELS; the solid dots are system members. The redshift range for these systems is 0.427 (top) to 0.534 (bottom).

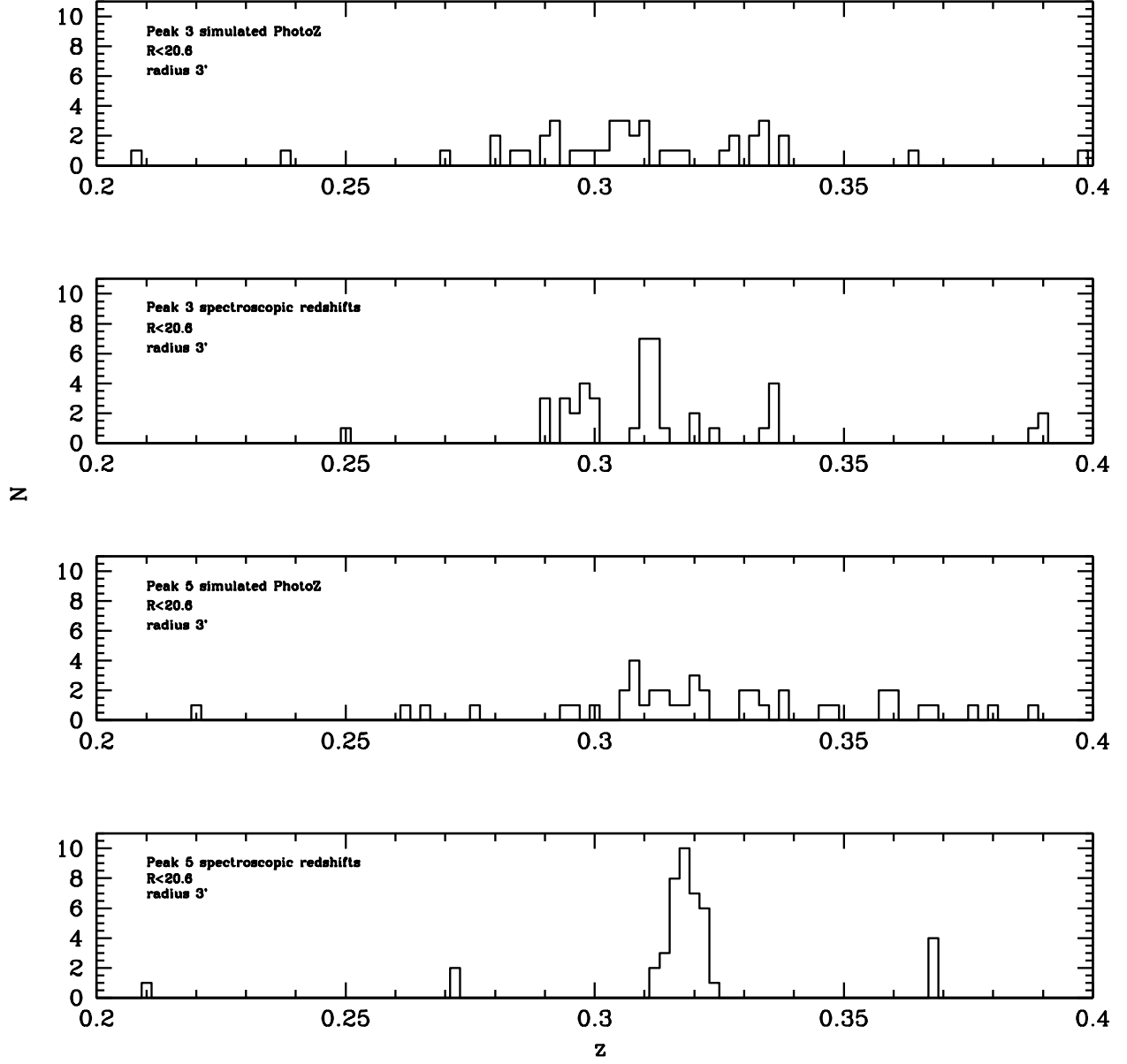


Fig. 16.— Impact of photometric redshifts on the ability to discriminate between a cluster of galaxies and a superposition of groups along the line-of-sight. The upper two panels show the distributions of perfect simulated photometric redshifts for convergence peaks 3 in the most populated redshift range 0.2 — 0.4 (top) and the true redshift distribution; the lower two panels show the perfect photometric redshift distribution for the cluster along the line-of-sight toward convergence map peak 5 (upper panel) and the true redshift distribution (lower panel). Note the similarity of the photometric redshift distributions and the marked difference between the true redshift distributions.